Chapter 3

Parametric Electron Oscillator

The parametrically driven motion from one electron in the hyperbolic Penning trap gives a large, clean signal and allows several new techniques. The bistability and hysteresis of this parametrically driven motion is exploited to create a detection scheme that has a one bit memory to store information about excitations performed 'in the dark', that is, without the detection amplifier turned on and without any drive (other than the cyclotron drive) that is able to make an appreciable increase in the particle's excitation amplitude. It is used to measure the cyclotron frequency to a one quantum resolution (one ppb), the precision needed to observe the electron spin flip. Furthermore, by taking advantage of the large signal and fast rise time of the parametric excitation, the rapid, enhanced spontaneous emission rate due to the surrounding microwave cavity is measured. The excitation risetimes are of particular interest in that they may provide a way to measure the temperature of a particle in a Penning trap. Finally, a parametric self-excitation scheme is investigated. This may provide a continuously monitorable, large oscillation signal at the particle's natural frequency. The hope is that the abrupt amplitude threshold characteristic of a parametric excitation makes the feedback loop less sensitive to noise below this threshold level. This self-excitation scheme may also permit better 'in the dark' detection.

The large, clean signal is made possible by the large harmonic volume and the

low background pressure. The large harmonic volume in an orthogonalized Penning trap allows the electron to be driven to a large axial amplitude, giving a large signal. Nonetheless, the slight distortions of the harmonic potential, quantified earlier as the Legendre expansion coefficients C_k, create bistability and hysteresis in the axial oscillations which are used in the above techniques. These distortions also prevent the particle's amplitude from increasing without bound, and thereby escaping the trap. It is possible to see this large oscillation only with a low background gas pressure. Previous signals from one electron parametric oscillations were limited by background gas atom collisions [92] which destroy the coherence of the oscillations. The present study has an extremely low background pressure, thereby permitting large, clean parametric signals that now display several characteristic features such as bistability and hysteresis. Parametric detection has been studied most extensively with large numbers of electrons in a Penning trap [78, 76, 29]. Here, the study is focussed on one particle.

Throughout this discussion of parametric oscillations in the hyperbolic Penning trap we shall assume that the slow magnetron motion (at frequency $\omega_m/(2\pi) = 13.6$ kHz) is cooled essentially to zero radius and is hence not an issue. The rapid cyclotron motion, also perpendicular to the magnetic field direction (5.3 Tesla), is at frequency $\omega_c'/(2\pi) = 148$ GHz. The axial motion, parallel to the magnetic field direction, is at frequency $\omega_z/(2\pi) = 63.4$ MHz.

3.1 Parametric Oscillator

The axial motion of an electron in a Penning trap is normally excited by a resonant drive, as discussed in the previous chapter. The particle can be parametrically excited instead by modulating the trapping potential at $\omega_d = 2(\omega_z + \epsilon)$. This gives a driven response at $\omega_z + \epsilon$. The one-electron parametric oscillator has the equation of motion,

$$\ddot{z} + \gamma_z \dot{z} + (\omega_z)^2[(1 + h\cos\ \omega_d t)z + \lambda_4 z^3 + \lambda_6 z^5] = 0. \tag{3.1}$$

The damping, at rate $\gamma_z^{-1} = 0.013$ s, is due to energy dissipated in the detection resistor. Tuning, by adjusting the compensation potential, changes the coefficients, λ_4 and λ_6, of the nonlinear terms. The λ_4 term can be tuned to zero; whereas the λ_6 term by design is close to zero, and has only a mild dependence on the compensation potential. Nonetheless, the slight residuals in these terms are responsible for arresting the parametric amplitude growth. In terms of the Legendre expansion coefficients discussed in Section 2.3, $\lambda_4 = 2C_4/(1+C_2)$ and $\lambda_6 = 3C_6/(1+C_2)$. We consider only these first two leading terms.

If we start with no axial excitation ($z = 0$), and increase the drive strength h, the nonlinear terms are not important initially since z is small, and we thus have only the familiar Mathieu equation with damping [1, 64]. An abrupt threshold occurs when the effect of the drive overcomes the damping at drive strength $h = h_T$ with

$$h_T = 2\gamma_z/\omega_z = 3.8 \times 10^{-7}. \tag{3.2}$$

(The number to the right is derived from the measured damping and axial frequency.) This threshold is illustrated in Fig. 3.1 for a parametric drive resonant at $\omega_d = 2\omega_z$ (i.e. $\epsilon = 0$).

According to the damped Mathieu equation, there is a sharply defined excitation range $\epsilon_- < \epsilon < \epsilon_+$ with

$$\epsilon_\pm = \pm\frac{1}{4}\omega_z\sqrt{h^2 - h_T^2} = \eta_\pm\omega_z, \tag{3.3}$$

where η is defined here to simplify later expressions. (The nonlinearity keeps the motions from expanding exponentially without limit but does not effect the excitation range.) Fig. 3.2 represents the excitation band $\epsilon_+ - \epsilon_-$ as a function of parametric drive amplitude. Fig. 3.1 and Fig. 3.3 correspond to vertical and horizontal slices through Fig. 3.2, respectively. Fig. 3.4 shows the measured excitation range (points) as a function of the drive strength, fit to Eq. 3.3 (line). From this fit we obtain $h_T = 4.3(\pm 1.1) \times 10^{-7}$, in good agreement with Eq. 3.2. If the parametric drive strength parameter is small ($h \ll 1$), then the steady-state solution,

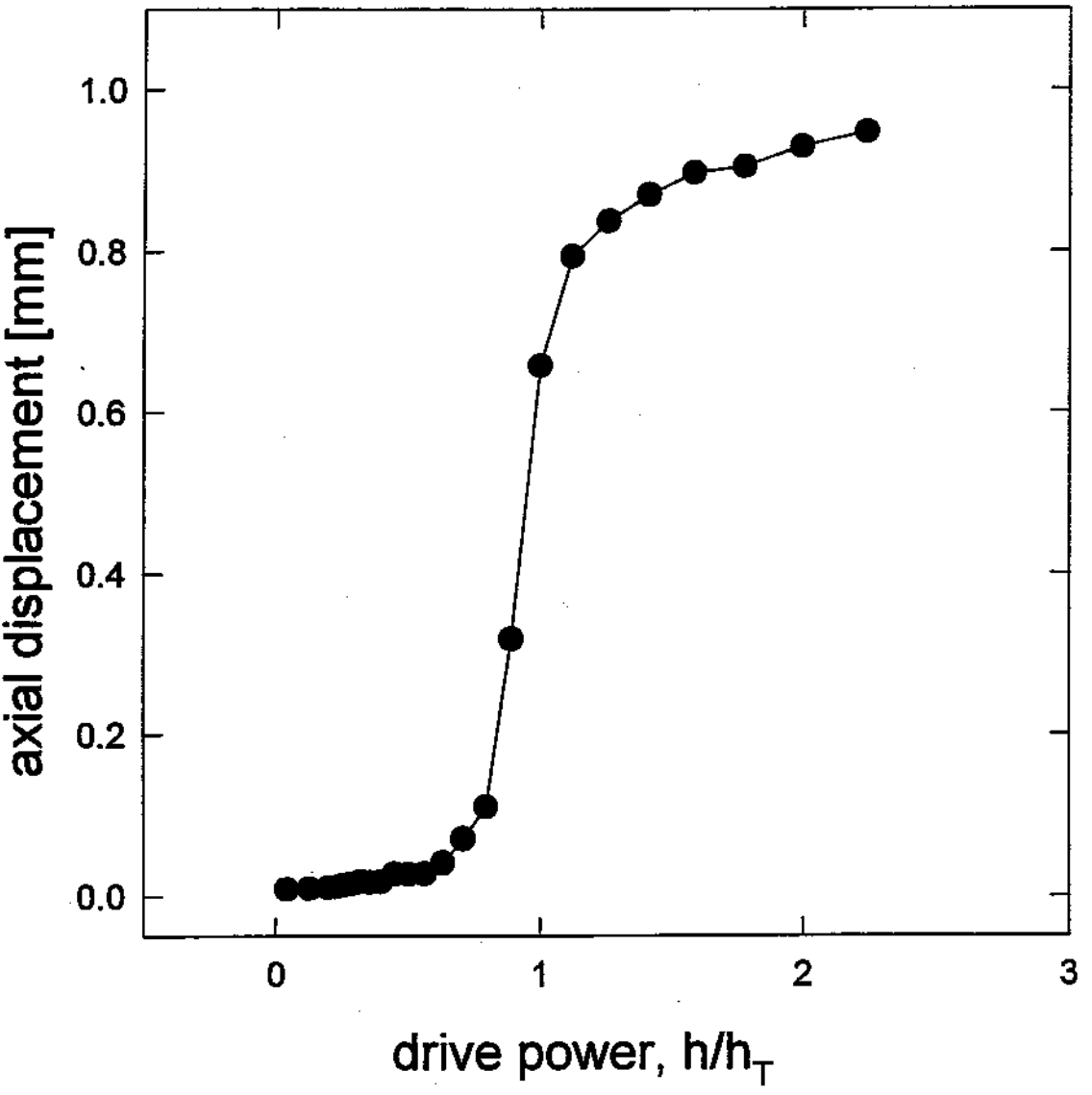

Figure 3.1: Measured amplitude of the parametric response at ω_z undergoes an abrupt threshold as the strength h of the parametric drive at $\omega_d = 2\omega_z$ is increased.

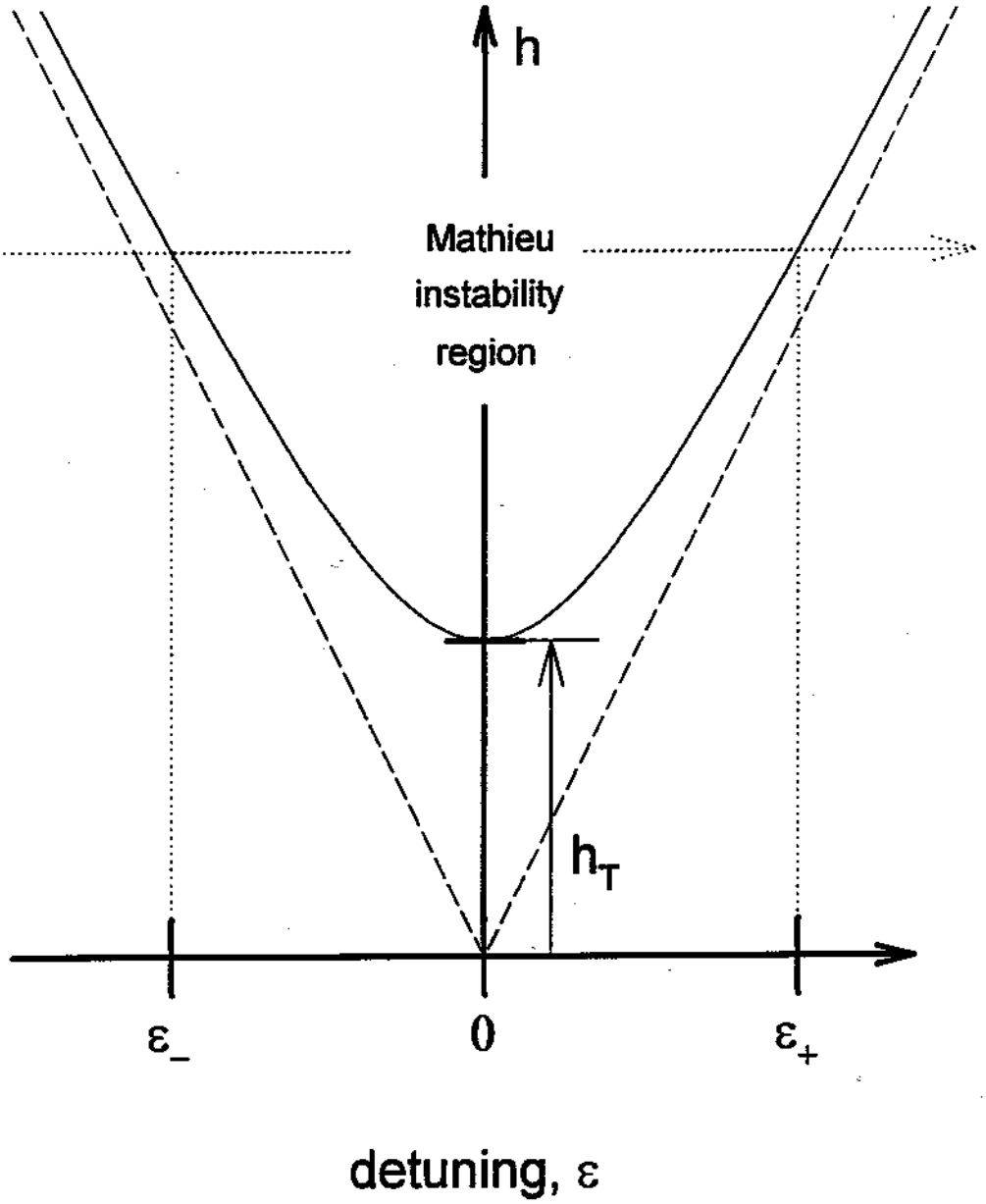

Figure 3.2: Excitation range $\epsilon_+ - \epsilon_-$ vs. parametric drive strength h for the Mathieu equation with damping. The amplitude of oscillation in the region of Mathieu instability will exponentially increase until limited by anharmonicities. Outside of this region, the steady state amplitude solution is zero.

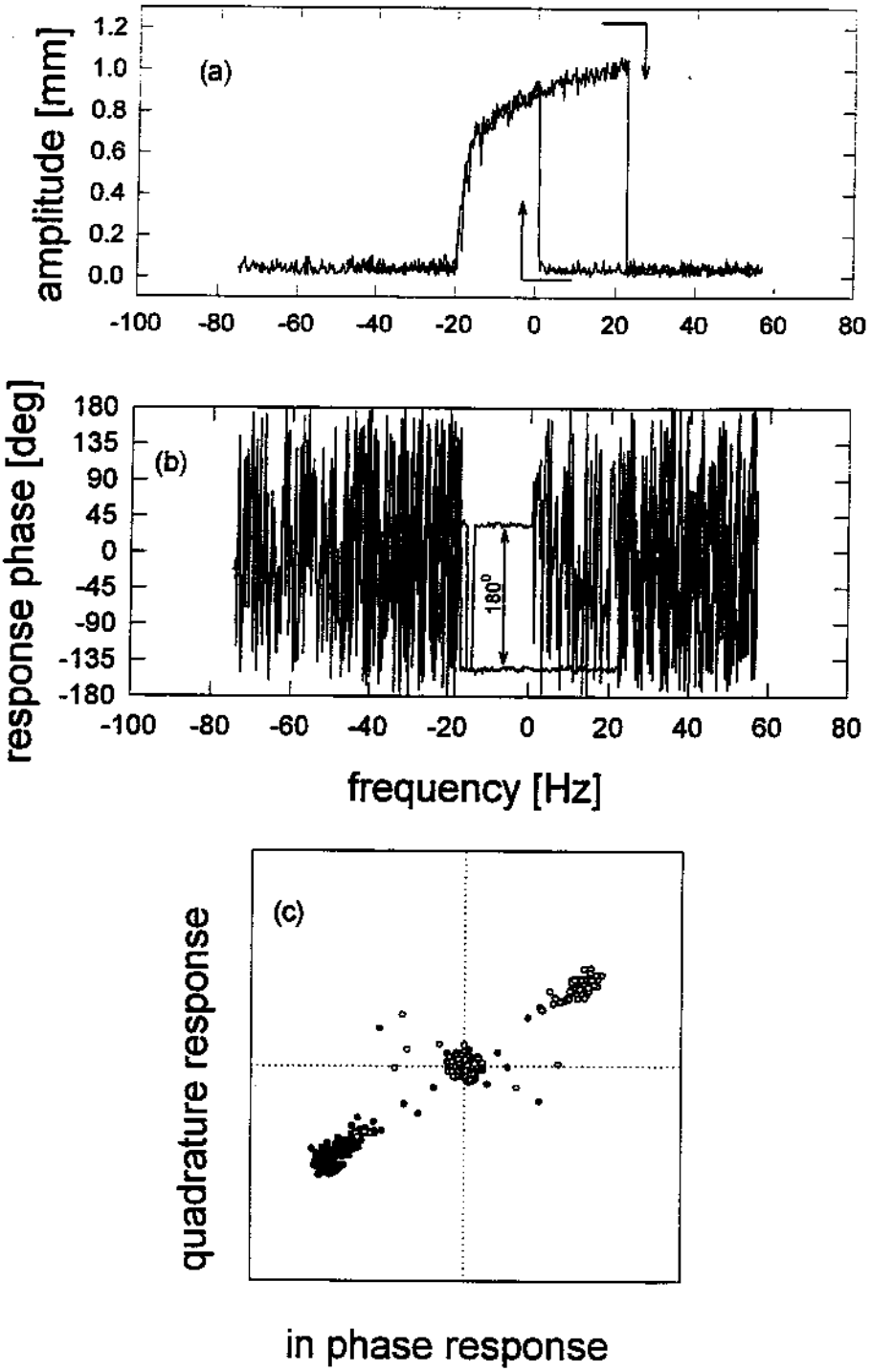

Figure 3.3: Amplitude (a) and phase (b) of the parametric response at $\omega_d/2 = \omega_z + \epsilon$ as the frequency of the parametric drive at ω_d is swept through resonance. The phase takes one of two bistable values near resonance and is not well defined off resonance where the response amplitude is very small, as is also illustrated in the measured phase space plot in (c).

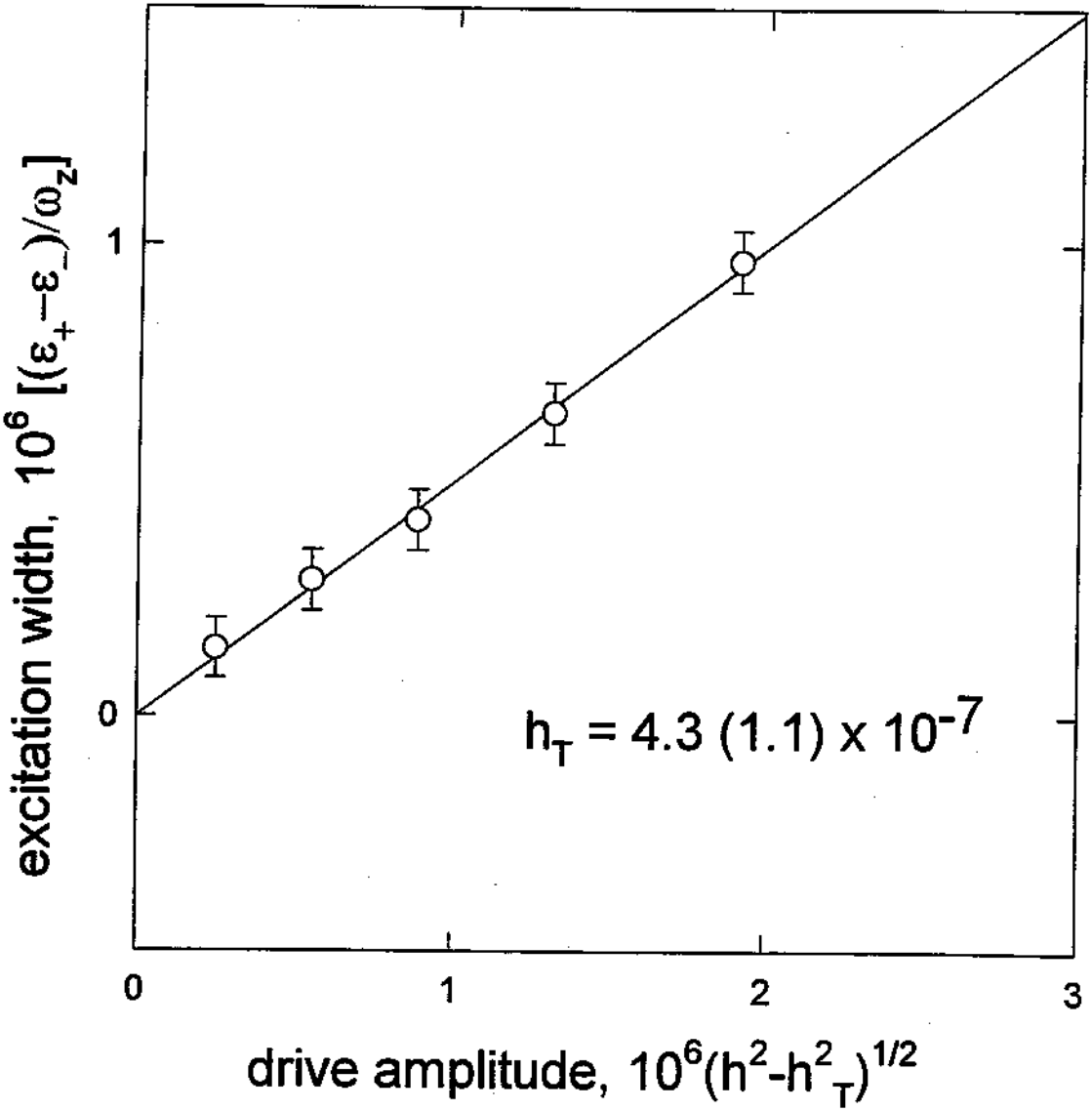

Figure 3.4: Excitation range $\epsilon_+ - \epsilon_-$ vs. parametric drive amplitude. This is used to determine h_T.

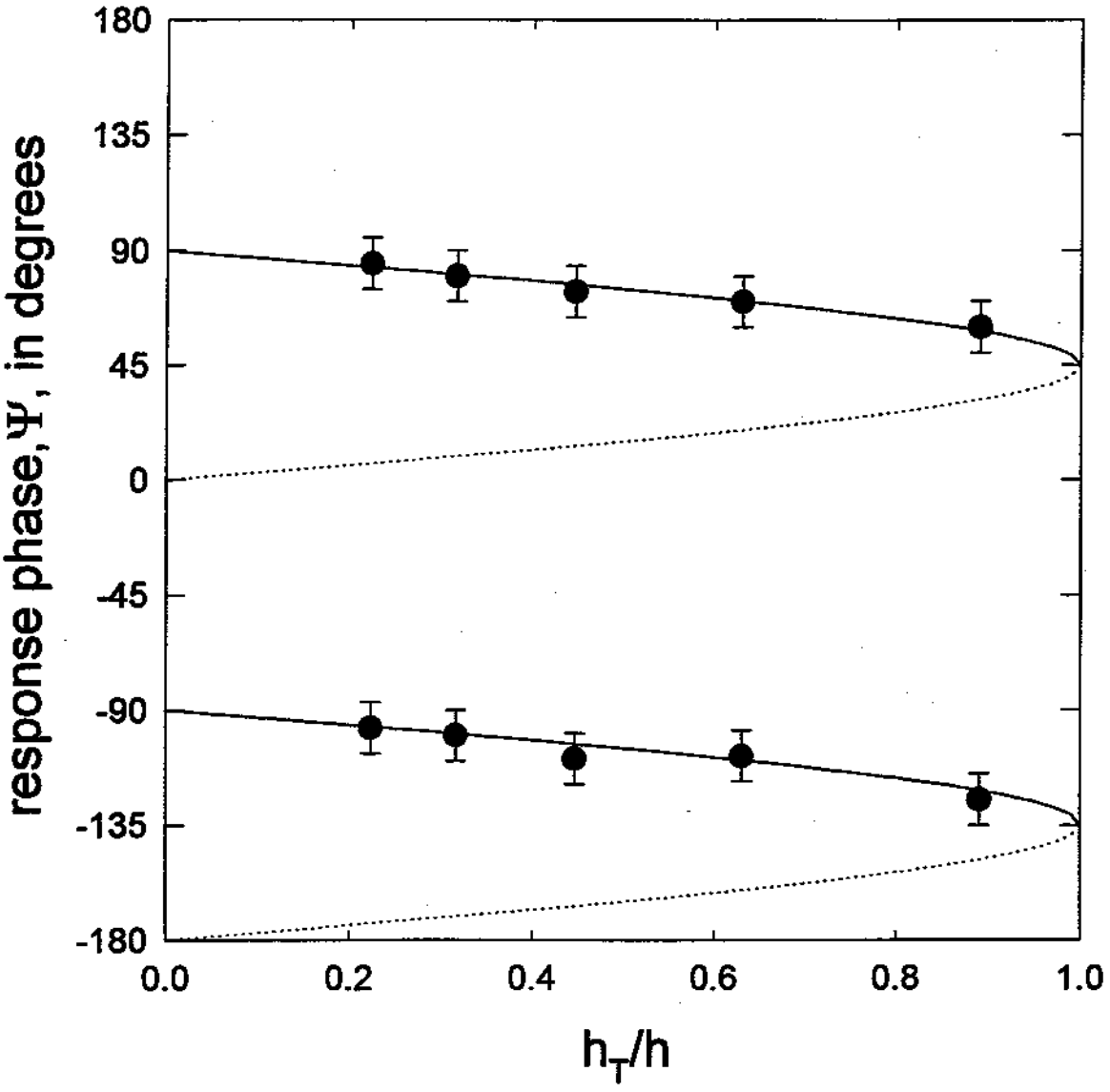

Figure 3.5: Measured phase of the parametric response (points) vs. drive strength. Solid curve is calculated phase for $C_6 > 0$; dashed curve for $C_6 < 0$.

$Z(t) = A(t)\cos[\Omega t + \Psi(t)] + O(h)$, satisfies the first order differential equations,

$$\frac{d}{dt}A(t) = -\frac{1}{2}\gamma_z[1 - \frac{h}{h_T}\sin(2\Psi)]A \tag{3.4}$$

$$\frac{d}{dt}\Psi(t) = (\omega_z - \Omega) + \frac{1}{4}\omega_z h\cos(2\Psi) + J, \tag{3.5}$$

where $J = \omega_z(\frac{3}{8}\lambda_4 A^2 + \frac{5}{16}\lambda_6 A^4)$ and $\Omega = \omega_d/2$. The steady state amplitude solution for a general combination of λ_4 and λ_6 is

$$\frac{5\lambda_6\omega_z}{16}A_\pm^4 + \frac{3\lambda_4\omega_z}{8}A_\pm^2 + \epsilon_\pm - \epsilon = 0. \tag{3.6}$$

The observed lineshapes can be fitted to these forms, and the values for the coefficients C_4 and C_6 can then be deduced. The steady state phase solutions are,

$$\sin(2\Psi) = h_T/h, \tag{3.7}$$

and

$$\cos(2\Psi) = \pm\sqrt{1 - (h_T/h)^2}, \tag{3.8}$$

where Ψ is the relative phase between the response and the drive. For a tuned trap where $C_6 > 0$ the - sign is stable; for $C_6 < 0$ the + sign is stable. The solutions are separated by 180 degrees. This reflects the time translation symmetry arising from the fact that the period of the driving force is half as long as the period of the response. For $C_6 > 0$, as is the case in the hyperbolic trap, the phase solution is restricted to the regions $\pi/4 < \Psi < \pi/2$ and $5\pi/4 < \Psi < 3\pi/2$, using the fact that h_T/h is defined to be greater than zero, as displayed in Fig. 3.5. Fig. 3.3 shows the amplitude and phase response as the parametric drive is swept in frequency. The phase is not well defined until the axial motion is excited to a nonzero amplitude near resonance. Near resonance, either of the two phases separated by 180 degrees is equally likely. One example of each phase is superimposed in the figure, and the amplitude and phase of all measured points are also displayed in a polar, phase space plot. Note that the phase remains near one attractor for a given excitation.

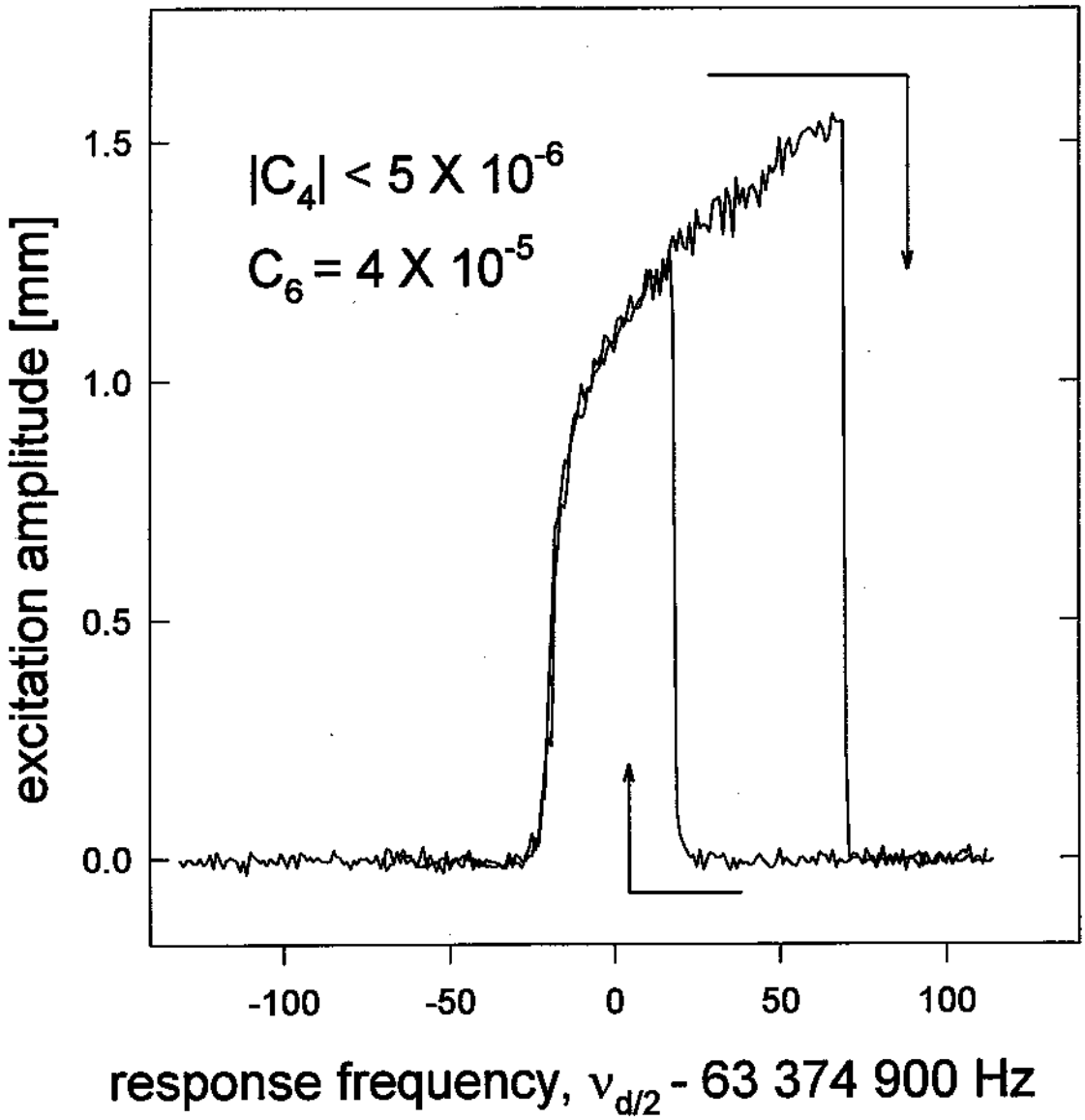

Figure 3.6: Amplitude of the parametric response at $\omega_d/2 = \omega_z + \epsilon$ as the frequency of the parametric drive at ω_d is swept through resonance, when the trap is tuned to make C_4 as small as possible. (Calibration of the mm scale depends on the calculated parameter, $D_4/D_6 = -5.2$ defined in Section 2.3.1.) Similar lineshapes have been observed for two electrons.

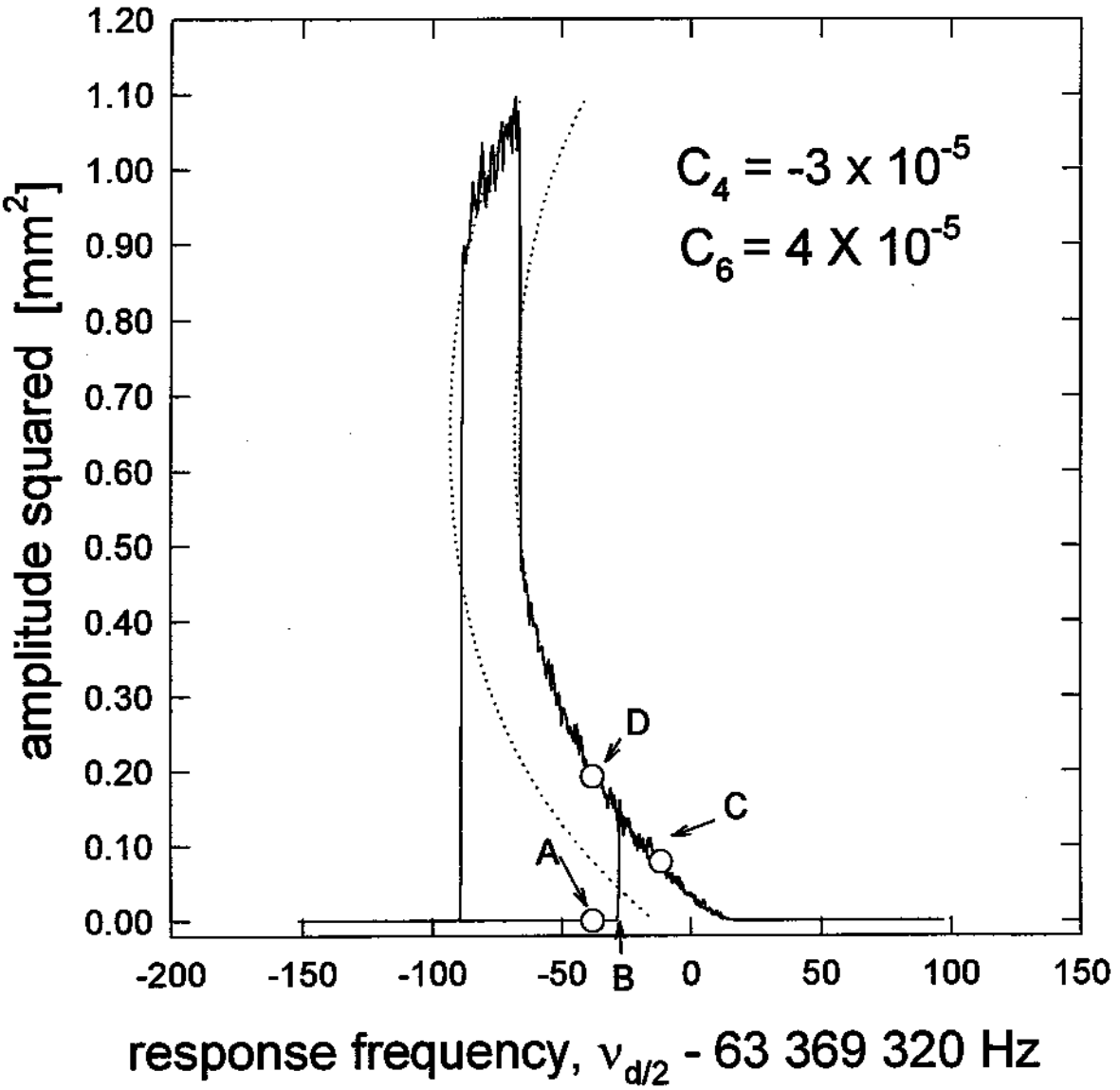

Figure 3.7: Amplitude squared of the parametric response at $\omega_d/2 = \omega_z + \epsilon$ as the frequency of the parametric drive at ω_d is swept through resonance, when the trap is mistuned to make C_4 and C_6 important. The dotted lines are a fit to parallel parabolas given in Eq. 3.6.

The measured line shapes exhibit bistability and hysteresis as illustrated in Fig. 3.6 where the line shape extends further when the drive is swept upward in frequency than when it is swept downward. The response in the double-valued bistable region thus depends on the excitation history. The trap was tuned in this case to make λ_4 as small as possible and the observed shape is determined by the value of λ_6. If the trap is deliberately mistuned to make λ_4 much larger, the excited line shape then becomes a straight line as is expected. If the trap is instead tuned so that both λ_4 and λ_6 are important, then a more complicated line shape results, one example of which is shown in Fig. 3.7. For parametric drives swept upward and downward through resonance, the measured amplitudes $A_\pm$ either vanish or lie on parallel parabolas (see Eq. 3.6) if we neglect higher order nonlinearities than those mentioned. This fit makes it possible to determine both C_4 and C_6 (or equivalently λ_4 and λ_6). In following sections we will illustrate how to use the bistability and hysteresis to record information about an excitation made "in the dark".

3.2 Anharmonicity Coefficients

The Legendre expansion coefficients may be determined by fitting the measured parametric lineshapes to Eq. 3.6, which can be rewritten to relate the signal strength, $S = \alpha A$, to the dimensionless detuning, $\eta = \epsilon/\omega_z$ and $\eta_\pm = \pm\frac{1}{4}\sqrt{h^2 - {h_T}^2}$. Here, A is the dimensionless amplitude, z/d, and α then is the proportionality constant between the observed signal and the amplitude of the oscillations. We then have,

$$\eta - \eta_\pm = \left(\frac{S}{\alpha}\right)^4 \frac{5}{16}\lambda_6 + \left(\frac{S}{\alpha}\right)^2 \frac{3}{8}\lambda_4. \tag{3.9}$$

This is a quadratic equation in S^2 with coefficients that depend on C_4 and C_6. (Recall that $\lambda_4 = 2C_4/(1 + C_2)$ and $\lambda_6 = 3C_6/(1 + C_2)$.) These in turn depend on the compensation potential V_c through the relation

$$C_k = {C_k}^{(0)} + D_k\left(\frac{V_c}{V_0}\right). \tag{3.10}$$

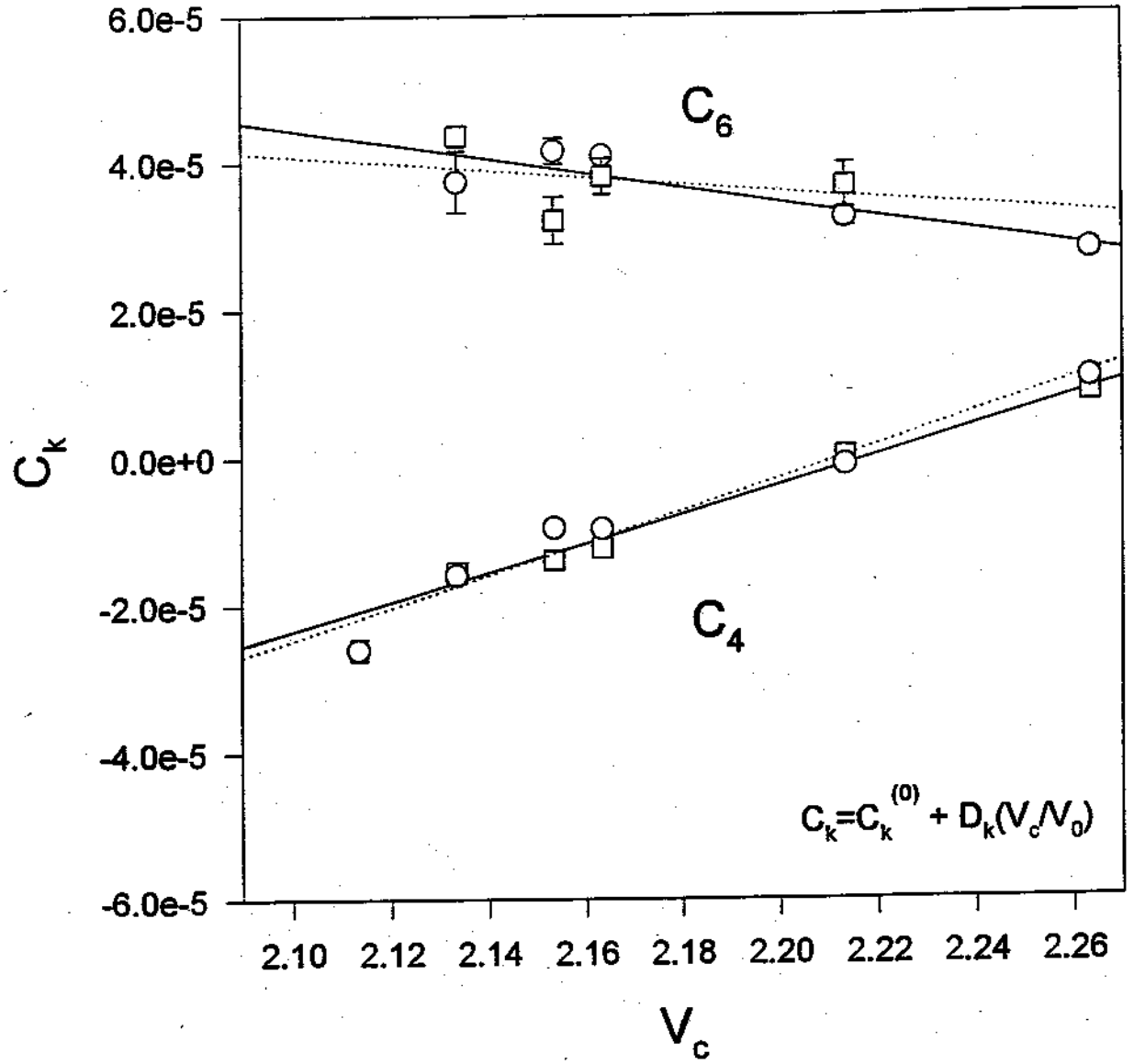

Figure 3.8: Measured C_4 and C_6 anharmonicity coefficients for two different drive strengths (dotted $h/h_T = 2.2$; solid $h/h_T = 3.2$) and a range of compensation settings.

The quadratic (a) and linear (b) coefficients of Eq. 3.9 are then functions of V_c,

$$\begin{aligned} a(V_c) &= \left(\tfrac{1}{\alpha^2}\right)\tfrac{3}{4(1+C_2)}(C_4) &= \left(\frac{1}{\alpha^2}\right)\frac{3}{4(1+C_2)}(C_4{}^{(0)} + D_4\frac{V_c}{V_0}) \\ b(V_c) &= \left(\tfrac{1}{\alpha^4}\right)\tfrac{15}{16(1+C_2)}(C_6) &= \left(\frac{1}{\alpha^4}\right)\frac{15}{16(1+C_2)}(C_6{}^{(0)} + D_6\frac{V_c}{V_0}). \end{aligned} \tag{3.11}$$

The variations of these coefficients with the compensation potential are given by

$$\begin{aligned} \frac{\Delta a}{\Delta V_c} &= \left(\tfrac{1}{\alpha^2}\right)\tfrac{3}{4(1+C_2)}\left(\tfrac{D_4}{V_0}\right) \\ \frac{\Delta b}{\Delta V_c} &= \left(\tfrac{1}{\alpha^4}\right)\tfrac{15}{16(1+C_2)}\left(\tfrac{D_6}{V_0}\right), \end{aligned} \tag{3.12}$$

and the zeros ($V_c = 0$) are related to the $C_k{}^{(0)}$ by

$$\begin{aligned} a(V_c = 0) &= \left(\tfrac{1}{\alpha^2}\right)\tfrac{3}{4(1+C_2)}C_4{}^{(0)} \\ b(V_c = 0) &= \left(\tfrac{1}{\alpha^4}\right)\tfrac{15}{16(1+C_2)}C_6{}^{(0)}. \end{aligned} \tag{3.13}$$

Thus, to extract the various Legendre coefficients from the parametric lineshapes we need to know the constant α. The ratio of D_4 to D_6 is much more well-known than the individual coefficients. We can take advantage of this to determine the value of α from the calculated ratio D_4/D_6. This gives from Eq. 3.12,

$$\alpha = \sqrt{\left(\frac{\Delta a/\Delta V_c}{\Delta b/\Delta V_c}\right)\frac{5}{4}\frac{D_6}{D_4}} = 0.48V/\text{mm}. \tag{3.14}$$

(The value of α obtained in this way, using the calculated ratio D_4/D_6, is better than the value $\alpha = 0.81V/\text{mm}$ obtained using just the calculated D_4[81].) The family of curves obtained with the drive strength and compensation tuning varied can then be fitted using the value of α to get values of C_4 and C_6. The results are shown in Fig. 3.8. That the C_4 points lie fairly well on a line and that the slope of the C_4 line, $D_4 = -2 \times 10^{-3}$, is in close agreement with the used calculated value indicates that the choice of α is good. The results are compared to the calculated values [35, 42] and are summarized in Table 3.1.

The amplitude calibration relates the signal voltage to the oscillation excursion. Therefore, we can estimate from the directly driven signal size that the typical

resonantly driven amplitude is $z = 0.29\,\mathrm{mm}$; and from the parametrically driven signal size that the typical parametric amplitude is $z = 1.0\,\mathrm{mm}$. (A 4.2K thermal amplitude would be $z = 0.03\,\mathrm{mm}$.) Thus, the resonantly driven amplitude is about 10 times the thermal amplitude; and the parametric amplitude is about 33 times.

The Legendre coefficient C_2 can also be measured by varying the trapping potential and recording the shift in the axial frequency.

$$\omega_z{}^2 = (1 + C_2)\frac{eV_0}{md^2} \tag{3.15}$$

This yields a value $C_2 = -0.0092(1)$, limited by the knowledge of the trap dimension, d.

There were discrete changes in the value of the Legendre coefficients over the several months of the measurement. A later determination of C_6 gave a value of 4×10^{-2}. This was associated with a new tune point (effective $\tilde{C}_4 = 0$). The parameters were such that it was not possible to get a reliable bistable region for one electron in order to perform dark detection, even when C_4 was used to cancel out C_6. The conflicting requirements that the trap be tuned (for good signal to noise) and that C_6 be small (for a distinct bistable region) demands that the overall value of C_6 be small. Perhaps a trap could be designed with a tunable C_6. The actual value can be checked using the above technique. In any case, these studies show that for parametric dark detection it is vital to have C_6 small.

3.3 Enhanced Spontaneous Emission

For the purposes of this discussion, because of special relativity, a cyclotron excitation to an energy E_c simply causes the axial frequency to shift,

$$\frac{\Delta\omega_z}{\omega_z} = -\frac{E_c}{2mc^2}, \tag{3.16}$$

and the cyclotron frequency to shift by,

$$\frac{\Delta\omega_c'}{\omega_c'} = -\frac{E_c}{mc^2}. \tag{3.17}$$

coefficients	hyperbolic calculated [35]	hyperbolic measured	cylindrical calculated [42]	cylindrical measured
C_1	0.75	-	0.78	-
C_3	0.27	-	0.32	-
$C_0^{(0)}$	0.00	-	-	-
$C_2^{(0)}$	-0.00	-0.009	0.1	-
$C_4^{(0)}$	-0.00	-0.000 5	0.1	-
$C_6^{(0)}$	0.00	0.000 2	-0.1	-0.1
D_0	0.008 7	-	-	-
D_2	-0.000 1	-0.000 3	0	0.000 02
D_4	-0.008 8	-0.002	-0.07	-
D_6	0.001 7	0.000 8	0.02	-
$\gamma_4 = D_2/D_4$	0.01	0.15	0	-0.000 3
$\gamma_6 = D_2/D_6$	-0.06	-0.38	-	-

Table 3.1: Summary of Legendre coefficients.

The dip to the right in Fig. 3.9 is the undriven axial resonance of a single electron observed for no cyclotron excitation. A cyclotron excitation of $E_c = 6.7$ eV causes the axial frequency to shift downward by 550 Hz (the left dip in Fig. 3.9). Turning off the cyclotron microwave drive causes the electron resonance dip to shift back to its original position as the cyclotron motion spontaneously emits synchrotron radiation. This spontaneous emission is modified by the presence of a surrounding microwave cavity which can either enhance or inhibit spontaneous emission [31, 62, 47, 53, 38].

For the large cyclotron excitations used here, the time it takes the axial resonance to come within a linewidth of its $E_c = 0$ position is of order 100 ms. However, since it takes several minutes of signal averaging to observe the dip in the noise resonance, it is not possible to time-resolve the shifting dip. One could apply a drive directly at ω_z for $E_c = 0$ and measure how long it takes to see the driven response illustrated in Fig. 2.12. Instead, we apply a parametric drive at $\omega_d = 2\omega_z$ and take advantage of the large signal which is rapidly produced by a parametric excitation. At time $t = 0$ the microwave drive is turned off and the cyclotron energy begins to damp. Special relativity shifts the axial resonance upward, eventually into parametric resonance with the drive. After a delay, a parametric response thus begins (much like those in Fig. 3.14). The response grows with a time constant that is due to a filter included to improve the signal-to-noise ratio. When this filter is removed, we can observe risetimes less than 10 ms, but the signal-to-noise ratio is such that averaging over hours then becomes necessary. Fig. 3.10 shows four measurements made of the time delay before a response is observed, for different values of the initial cyclotron excitation. Each point is an average of 10 trials. The fitted line (constrained to pass through the origin) gives an exponential damping time for the cyclotron motion of 43 ± 4 ms. In free space, this cyclotron radiation lifetime would be 99 ms so the spontaneous emission is clearly enhanced by the coupling between the cyclotron motion and the trap cavity. In the past, only longer damping times for inhibited spontaneous emission could be observed [38] because the method was limited by the detection response time. The shift in the cyclotron energy was measured (in a

window on the order of the damping time) after a delay. The ratio of the energy shift to the delay gives the emission rate. Therefore, cyclotron energies that decay faster than the measurement window time will not be resolved. In contrast, the present scheme measures the total time of decay for a known energy shift. The total time of decay is long compared to the response time of the detection circuitry. Thus, the measurement is not limited by the detection response time. To measure the frequency dependence of the emission rate, the magnetic field has to be changed. (The cyclotron oscillator frequency is proportional to the magnetic field strength.) This entails waiting over a week between field changes to allow the solenoid to stabilize enough to make a measurement. (Up to a month is typically needed to stabilize to one ppb.) In the present setup, a normal current coil with a large field range can be used to vary the cyclotron oscillator over the lineshape of a cavity mode (see Chapter 4).

3.4 Parametric Dark Detection

The measured enhanced spontaneous emission rate reported in the last section was done "in the dark" insofar as the cyclotron decay occurred in the absence of any drive able to make an appreciable increase in the electron's excitation amplitude. However, the FET amplifier which detected the voltage induced across the resistor was left on continuously and energy dissipated in this FET caused the effective temperature of the resistor R to be greater than the ambient 4.2 K. (Previously, the estimated axial temperature was 32 K [26].) We now consider a cyclotron frequency measurement which is more "in the dark" insofar as the FET detection amplifier is turned off during the crucial part of the measurement, allowing the resistor temperature to decrease to the ambient 4.2 K. The parametric axial oscillator is used as a one bit memory to record whether or not a cyclotron excitation occurred. Since special relativity produces a shift in the electron's axial frequency when the cyclotron motion is excited, we need only detect a shift in the axial frequency. A parametric drive is

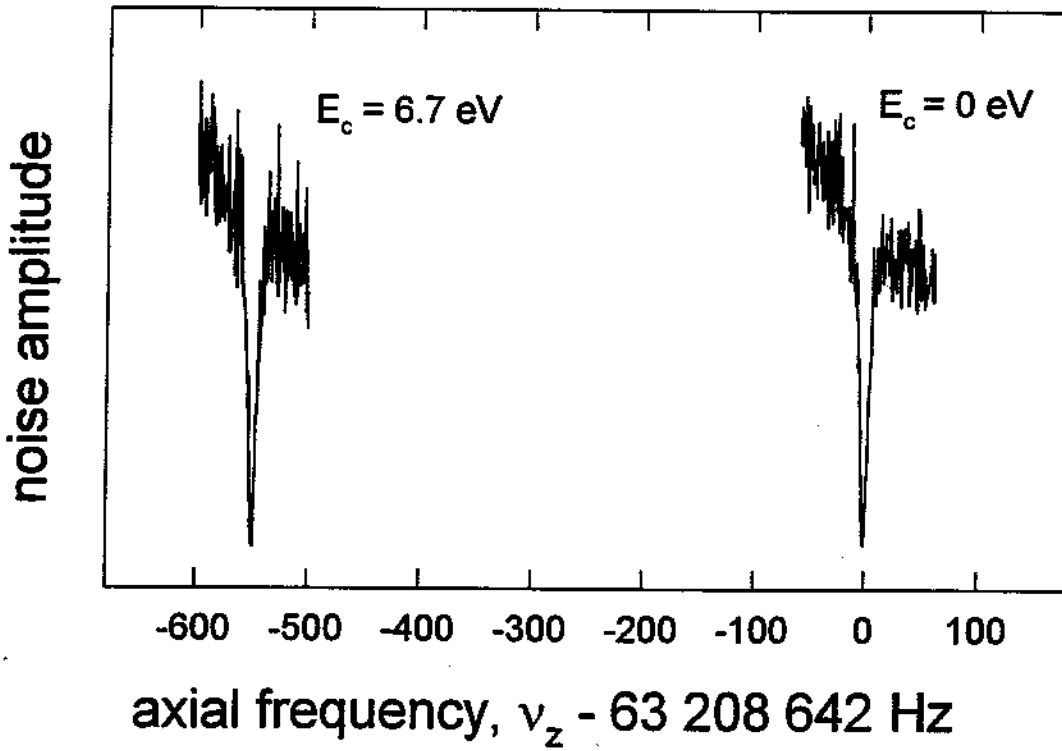

Figure 3.9: Axial resonance of a single trapped electron (noise-shorting dip to the right) is shifted to a lower frequency (left) when the the electron's cyclotron motion is excited to an energy of $E_c = 6.7$ eV. When the cyclotron drive is turned off, the dip shifts back as the electron damps via its coupling to the radiation field in the trap cavity.

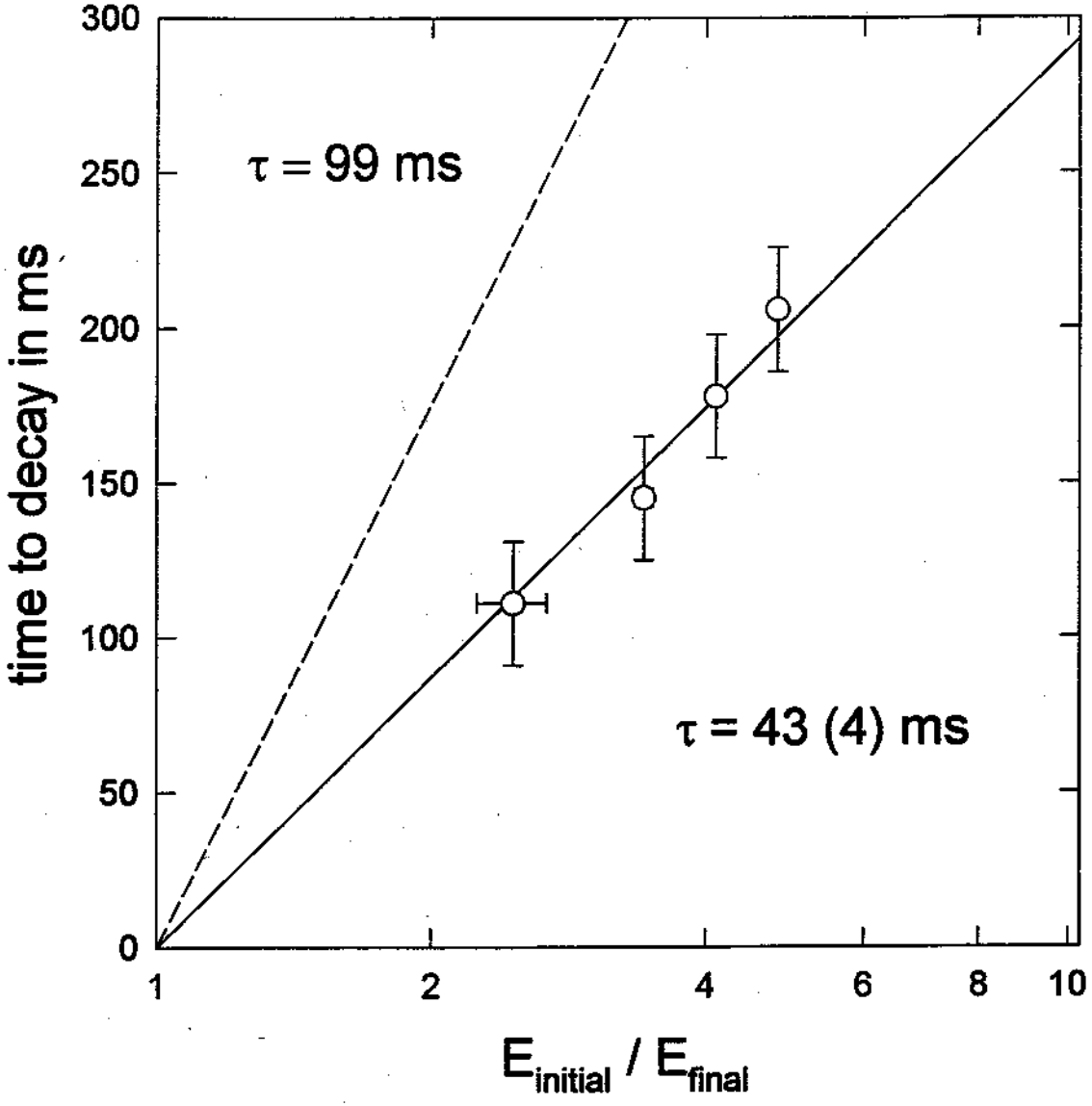

Figure 3.10: Time between turning off the cyclotron drive and the first observation of a parametric axial response, as a function of the energy of the initial cyclotron excitation. The fitted line (constrained to pass through the origin) shows an exponential damping time for the cyclotron motion which is shorter than the spontaneous emission time in free space (dashed line). Spontaneous emission is enhanced by the coupling of the electron cyclotron motion and the cavity.

turned on at a frequency corresponding to point A in Fig. 3.7. The axial motion of the electron is not excited. A downward, relativistic shift in the electron's axial frequency is equivalent to shifting the frequency of the parametric drive upward to point C in the figure. The electron's axial motion remains unexcited during the initial (and critical) cyclotron excitation, until the electron enters the single valued region at arrow B enroute to point C. Even when the axial frequency shifts back because the cyclotron drive is turned off, the parametric hysteresis makes the axial excitation persist as indicated by point D in the figure. The FET detector is subsequently turned on to read out the one bit memory, to find out whether an axial frequency shift (and hence a cyclotron excitation) took place.

To make a cyclotron excitation, a cyclotron drive frequency is swept upward to a *turningpoint* and then back downward [24] as shown in Fig. 3.11. If the turning point is higher in frequency than the unshifted cyclotron frequency, a large excitation is expected (like that directly detected with the FET turned on). If the turning point is less than the unshifted cyclotron frequency (and there is no power broadening) then no excitation is expected (see Fig. 3.11). This relativistic anharmonic cyclotron oscillator will be described in the next chapter. Fig. 3.12 shows the probability of observing a large excitation as a function of turning point frequencies which are separated from each other by one part in 10^9 (1 ppb). Each point is the average of 10 trials. It took two hours to produce this curve owing largely to the time required to turn on and off the heavily filtered voltage supply for the FET. The observed edge is very clean and has a resolution width less than 1 ppb. This resolution of 1 ppb corresponds to the relativistic frequency shift due to a single quantum excitation of the cyclotron oscillator. Since no spin is flipped we focus on one of the two "ladders" of Landau levels. The cyclotron energy levels are discussed in the next chapter. Because of special relativity the cyclotron energy levels are not equally spaced. Instead, the transition frequency between successively higher pairs of energy levels is lower by

$$\delta = \frac{\hbar(\omega_c')^2}{mc^2}, \tag{3.18}$$

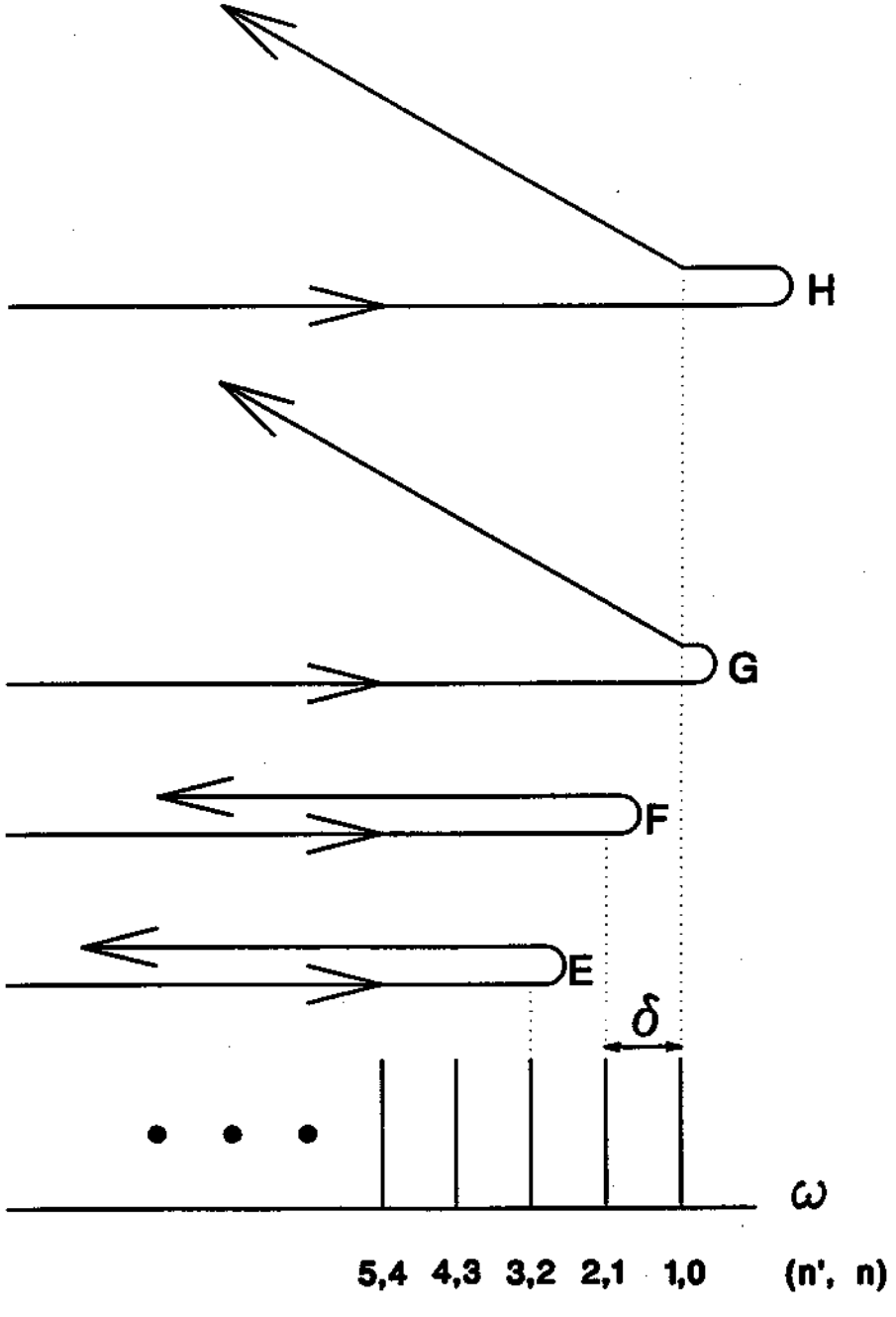

Figure 3.11: Representation of anharmonic relativistic excitations of the cyclotron motion of one electron as the cyclotron drive is swept up to a turning point and then back down to lower frequencies. Points E and F will not produce and excitation; whereas, points G and H allow large excitations. For reference, the Landau ladder resonant frequencies are shown below.

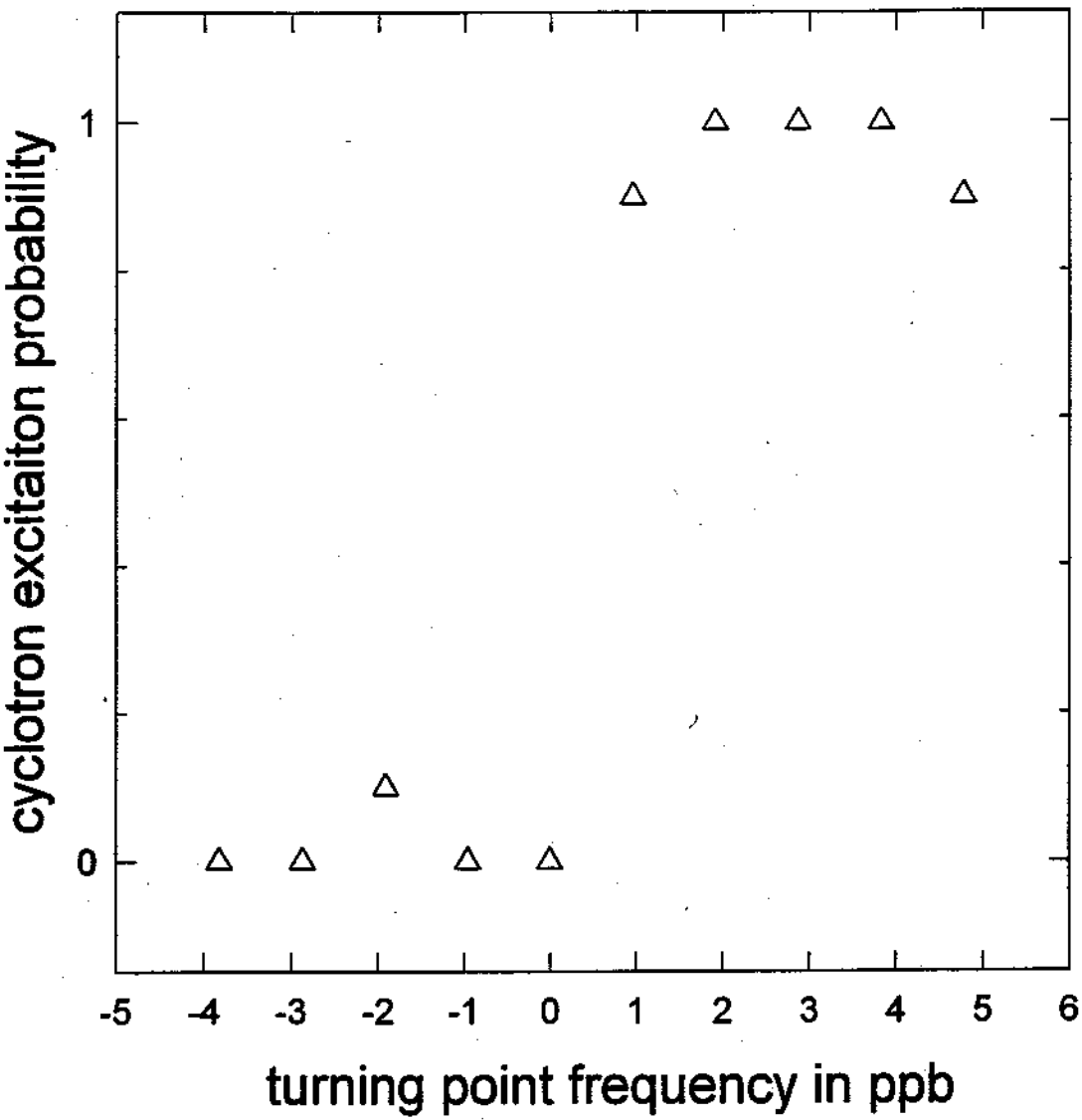

Figure 3.12: Probability for anharmonic relativistic excitation of the cyclotron motion of one electron as a function of the turning point frequency from which the cyclotron drive is swept to lower frequencies. Each point is an average of ten trials. The observed resolution is 1 ppb.

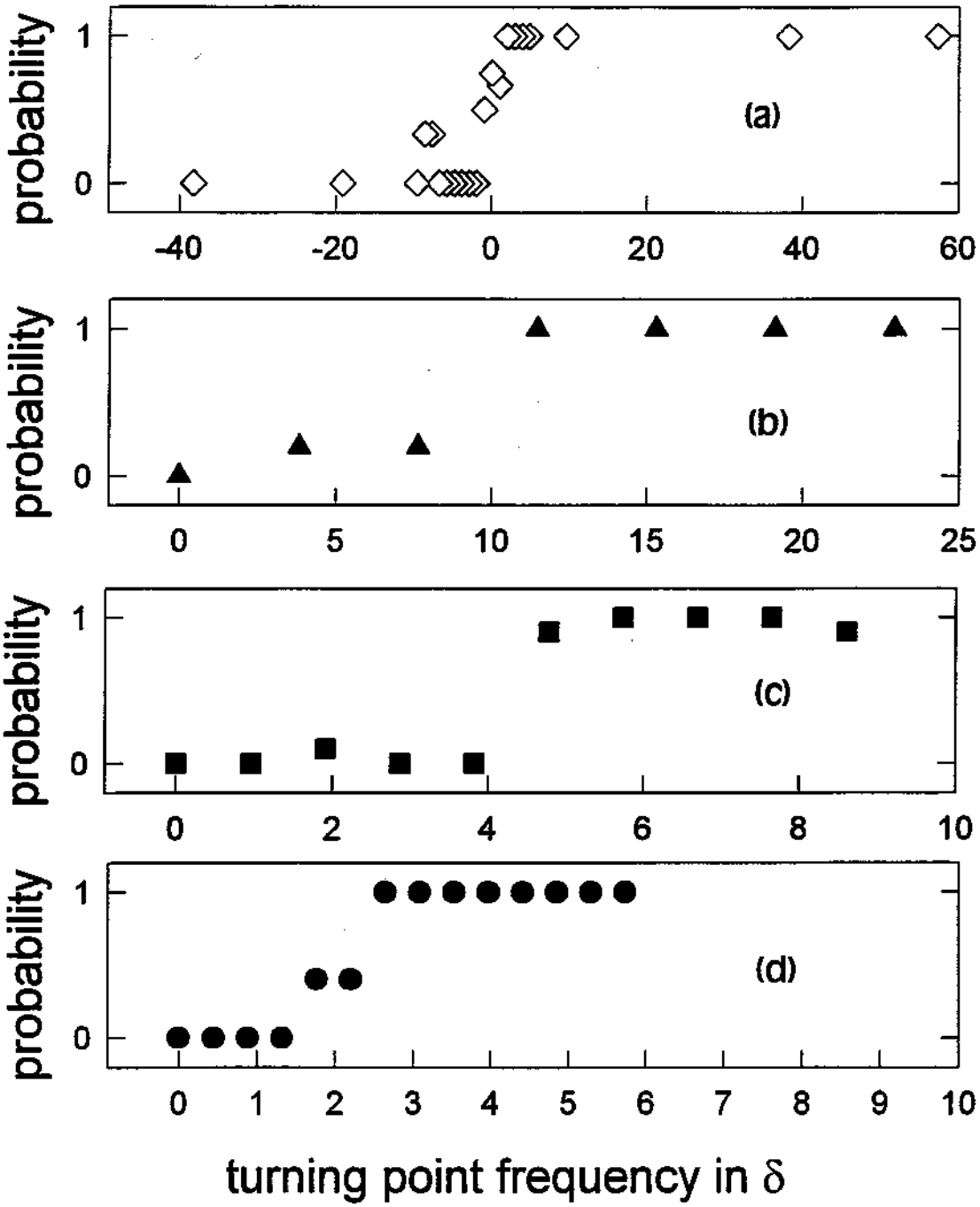

Figure 3.13: Probability for anharmonic relativistic excitation of the cyclotron motion of one electron as a function of the turning point frequency from which the cyclotron drive is swept to lower frequencies. Graph (a) is obtained using conventional resonant axial drives. Graphs (b)-(d) use dark detection with finer frequency increments.

where $\delta/\omega_c' = 10^{-9}$. We have thus succeeded in resolving a one quantum excitation of the cyclotron motion using special relativity, without resorting to any magnetic field inhomogeneities which couple the various electron motions and severely broaden the resonance line shapes [85, 68]. This resolution also indicates that the magnetic field produced by the self-shielding, superconducting solenoid [44] drifted less than 1 ppb during this particular 2 hour measurement. The measurement was taken after 2 AM on New Year's Day during a heavy snowstorm. Typically, magnetic field fluctuations are smallest between 1:30 AM and 5:30 AM when the MBTA subway is shut down. Fig. 3.13 illustrates a conventional resonant drive detection of the cyclotron 'edge' and three dark detection measurements with increasing resolution. The conventional detection maintains a direct resonant axial drive on the particle. The shift in the axial frequency can then be continuously monitored. Graph (a) shows the average of four measurements as the cyclotron frequency turning point is stepped across the cyclotron edge. This is not 'in the dark' in the sense that the FET is on and that the resonant axial drive is also on. The precision obtained is about 3 -10 ppb. This is comparable to the 2.5-7 ppb resolution over a few hours obtained using clouds of 50-100 electrons. Graphs (b)-(d) show three different 'dark' measurements with increasing resolution. Graphs (b) and (d) were the average of five trials per point, while graph (c), discussed above, is the average of 10 trials per point. The precision obtained is 1-1.3 ppb.

For a completely "in the dark" experiment, the axial motion must also be decoupled from the thermal noise from the detection resistor. This is easily accomplished by detuning the trap potential to make the axial frequency no longer resonant with the LCR circuit which the resistor in Fig. 2.9 represents. However, the axial excitation will remain at the average energy corresponding to 4.2 K insofar as such detuning also eliminates the axial damping. To cool the axial motion below 4.2 K, it should be possible to employ cavity sideband cooling [37]. At the 4.2 K ambient temperature of our current traps, the cooling limit for the axial motion would be 2 mK. If we succeed in lowering our ambient temperature to 20 mK (an apparatus

in our laboratory without the trap installed has already reached 17 mK), then the axial energy would be reduced to only 9 μK.

3.5 Excitation Risetimes

So far we have considered only the steady state line shapes. It is important to realize, however, that the time it takes to reach the steady state excitation amplitude depends upon the detuning ϵ of the drive from the resonant frequency. As the excitation begins from zero amplitude, the amplitude initially increases exponentially with the time constant τ given (within the excitation range) by

$$\tau^{-1} = \sqrt{\epsilon_{\pm}^2 - \epsilon^2 + (\gamma_z/2)^2} - \gamma_z/2 = \frac{1}{4}\omega_z[\sqrt{h^2 - (4\epsilon/\omega_z)^2} - h_T], \quad (3.19)$$

which is determined solely by the damped Mathieu equation. As the amplitude increases, however, the nonlinearity becomes increasingly important and eventually arrests the exponential growth. Fig. 3.14 illustrates how the response amplitude grows as a function of time with $t = 0$ being the time at which the parametric drive is turned on. The response has a 10 ms delay due to a filter. For the detunings shown, the risetimes as calculated from Eq. 3.19 are between 7 and 13 ms. This is consistent with the plots shown in Fig. 3.14. The 10 ms filter can be removed, but the averaging time becomes several hours. A resolution of about 2 ms can be obtained in this way (faster than the axial damping time of 13 ms). Fast time resolution is useful for measuring shifts into the excitation band. In order to get substantially longer risetimes, which are useful for amplitude growth studies, the detuning has to be closer than $\gamma_z/2$ of the excitation edge, $\epsilon_{\pm}$. This requires that the resonance lineshape be stable over the averaging time scale. Note from Eq. 3.19 and 3.3 that the risetime within the excitation range can be decreased as desired by increasing the drive strength h and can be increased by moving to the ends of the excitation range(see Fig. 3.15 and Fig. 3.16). The time taken to excite to a steady state will also depend in a very sensitive way upon the initial thermal excitation amplitude,

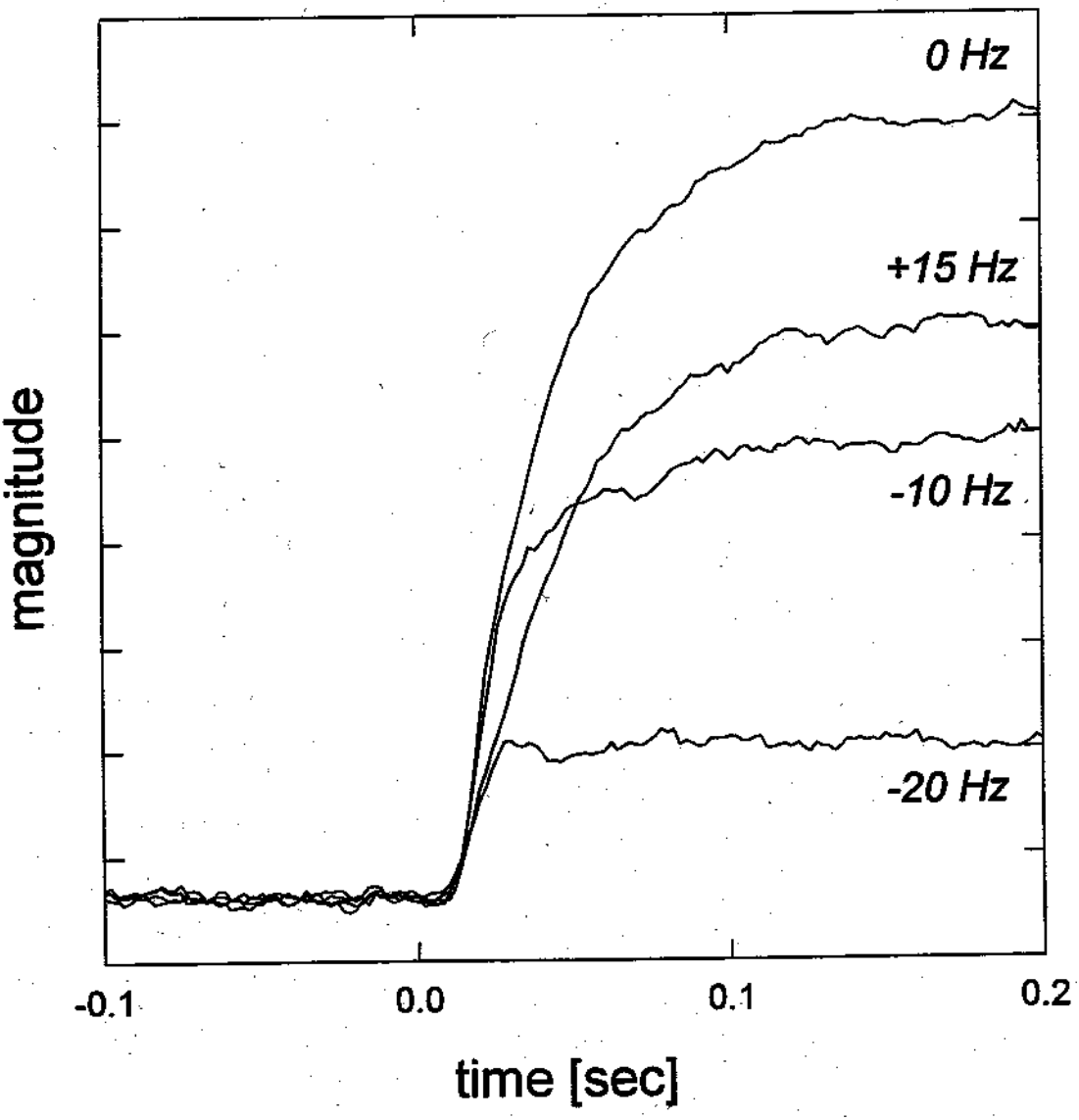

Figure 3.14: Risetime of parametric excitation for detunings: +15 Hz, 0 Hz, -10 Hz, and -20 Hz. The cryostat warmed up during the average of the 0 Hz curve.

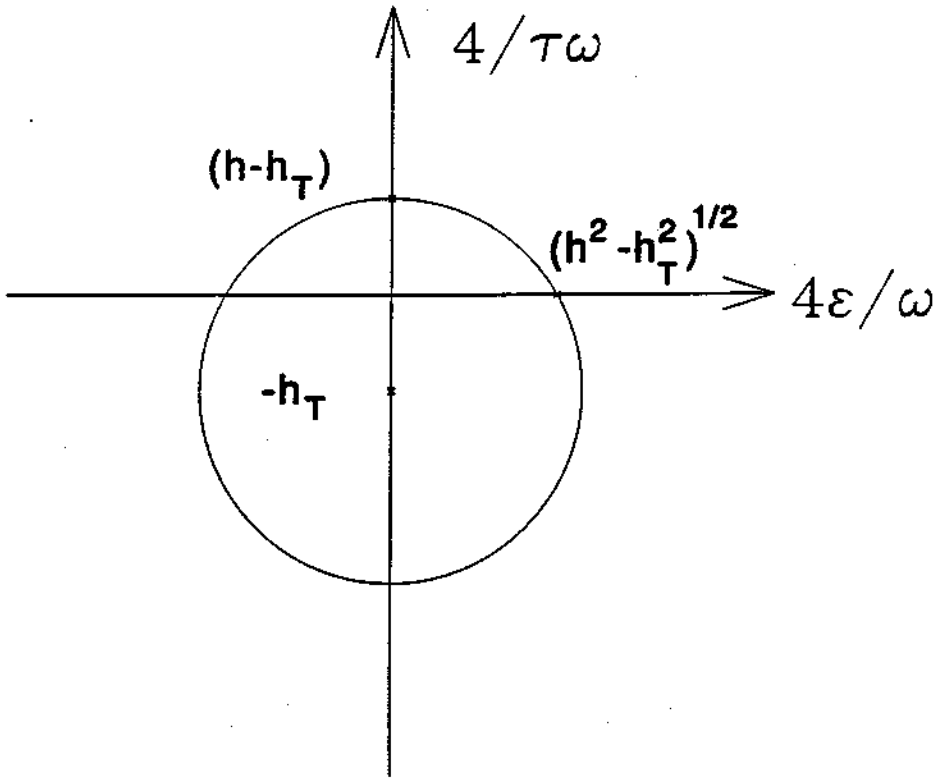

Figure 3.15: Calculated excitation risetime inverse as a function of detuning, given by Eq.3.19. Only positive times are valid.

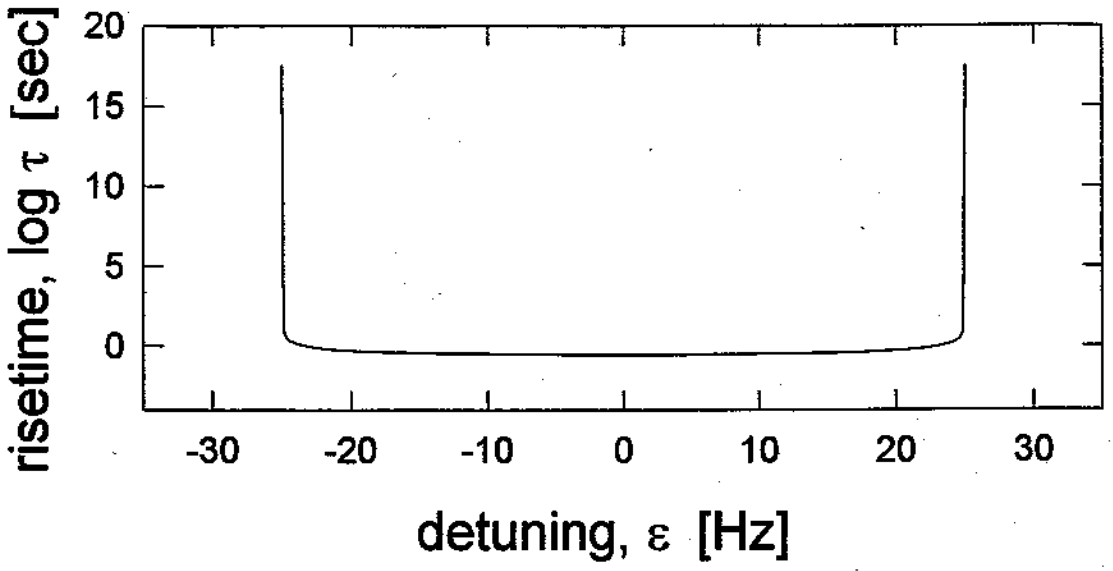

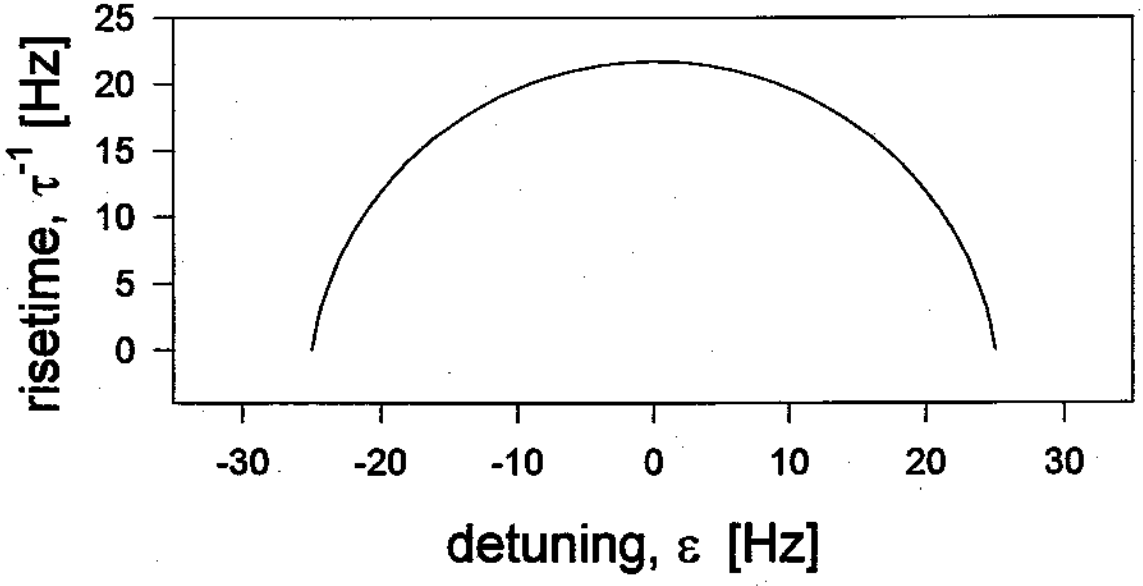

Figure 3.16: Calculated excitation risetime as a function of detuning for the experimental parameters. For detunings within $\gamma_z/2$ of the excitation band edge, substantially longer risetimes are possible.

suggesting excitation time measurements as a promising way to measure axial temperature of a single particle, or several particles. (See also [95] for a discussion on using a fixed parametric drive pulse as an amplifier.)

It is interesting to compare this behavior to that of a directly driven oscillator which has a linear rather than an exponential growth behavior. There is an amplitude limit if the drive is off resonance, or if there is damping. With damping, the approach to equilibrium is on the order of a damping time. Therefore, it may also be possible to use a direct drive to measure the temperature of a particle. This forgoes the advantage of the parametric excitation which can have risetimes that are much longer than the damping time.

3.6 Self-Excitation

The possibility of a self-excited oscillator may be realized by amplifying the signal from a trapped particle and then feeding it back to drive the particle [27]. Here, we instead feed back the large signal from a parametrically excited electron. Because of the drive strength threshold the electron will not respond to noise voltages below that threshold, but only to the fedback signal which is adjusted to be above the threshold. Furthermore, the anharmonicity limited amplitude makes the system less sensitive to the exact gain setting in the feedback loop. The phase of a parametric response also varies little over the excitation range (Fig. 3.3). Also, the phase variation for different drive strengths is weak (Fig. 3.5). The two 180° response phase solutions generated in the feedback loop act as drives that will continue the excitation. This robustness in the feedback conditions for excitation makes it easy to configure the system for an excitation; however, it also allows noise to excite the amplitude of the particle. By adjusting the two local oscillators (LO #1 and LO #2) one can determine whether the excitation response is due to noise or due to a resonant parametric feedback. The scheme (shown in Fig. 3.17) takes the 63 MHz response signal from the electron and mixes it by LO #1 to a signal at about 5 MHz. This

is then mixed to 126 MHz and fedback to the trap as a parametric drive. Only one frequency will satisfy the doubled frequency criteria, $\omega_{drive} = 2\omega_{response}$. This then strongly filters the parametric feedback drive. The observed signal is derived from the 5 MHz IF which is mixed to 90 kHz and detected on an audio spectrum analyzer. This is similar to optical soliton generation.

Two responses were observed from the parametric feedback setup: a noise response (Fig. 3.18) and a resonant feedback response (Fig. 3.19). These may be distinguished by varying the two local oscillators. Suppose the electron response is at ω_z. If LO #1 is shifted from $\omega_z - 5\text{MHz}$ to $\omega_z - 5\text{MHz} + \Delta$, then the parametric feedback will shift from $2\omega_z$ to $2\omega_z - \Delta$. (The frequency of LO #2 is set at $2\omega_z - 5\text{MHz}$). This drive will, in turn, produce an excitation at $\omega_z - \Delta/2$. Iterating this circuit, the response will settle at a frequency $\omega_z - \Delta \sum_{n=1}^{\infty} \left(\frac{1}{2}\right)^n = \omega_z - \Delta$. The response frequency is then mixed with LO #1 to give an IF frequency of 5 MHz-2Δ, which is then mixed with 5.090 MHz to give an audio signal at 90 kHz +2Δ. The audio signal will then be shifted by +2Δ. Therefore, the detected audio response will have a slope with variation in LO #1 of 2. In contrast, a noise excited response will not depend on the frequency of the fedback signal, and thus will have a slope of 1 with respect to the LO #1 frequency. This is shown in Fig. 3.20. Similarly, if the frequency of LO #2 is shifted from $2\omega_z - 5\text{MHz}$ to $2\omega_z - 5\text{MHz} + \eta$, the response will be at $\omega_z + \eta/2$. This will then generate a parametric feedback drive at $2\omega_z + \eta + \eta/2$. Continuing this gives a settled response frequency of $\omega_z + \left(\frac{\eta}{2}\right)\left[1 + \frac{1}{2} + \left(\frac{1}{2}\right)^2 + \cdots\right] = \omega_z + \eta$. Therefore, the audio signal will have a slope with variation in LO #2 of -1. The noise excited response will not depend on the exact frequency of LO #2, and thus will have a slope of zero. This is shown in Fig. 3.21. To avoid aliasing, LO #1 was offset by -200 Hz, and LO #2 was offset by -100 Hz. Finally, the resonant excitation will not change with a change in the trapping potential whereas the noise driven excitation will. This is observed.

A frequency doubled ($2\omega_z$) parametric scheme and a direct (ω_z) feedback scheme were tried, but without success. The limiting factors seemed to be the power needed

to saturate the frequency doubler element and the bandwidth of the processing filters. These should be readily surmountable. This would give a self-excited oscillator without a predetermined frequency which would allow a precise and continuous monitoring of the particle frequency. This would then provide a possible frequency standard, or a sensitive detector of slight frequency shifts due to specific processes. These oscillations would be insensitive to the harmonic quality of the trap. Preliminary calculations suggest that it may be possible to construct a feedback that is stable, and that allows monitoring of the natural frequency of the particle. The demonstrated parametric feedback scheme, on the other hand, has a frequency determined by LO #2. This has the advantage of being highly frequency selective, but the disadvantage that we learn nothing about the electron's resonant frequency within the parametric excitation band. This might be exploited to serve as a better dark detection scheme. Suppose the apparatus is configured to give a parametric resonance as in Fig. 3.7. Now, if the parametric feedback is adjusted to be resonant at point A, the particle will experience no drive whatsoever. If the natural axial frequency shifts past point B (due to a cyclotron excitation, for instance), the amplitude will quickly increase due to the feedback. (This unfortunately requires the FET to be on.) Because the particle is not excited, and there is no external drive this detection configuration would be more in the dark. Depending on the stability of the trapping parameters, this may allow precise frequency shift discrimination. Other possible applications include particle cooling.

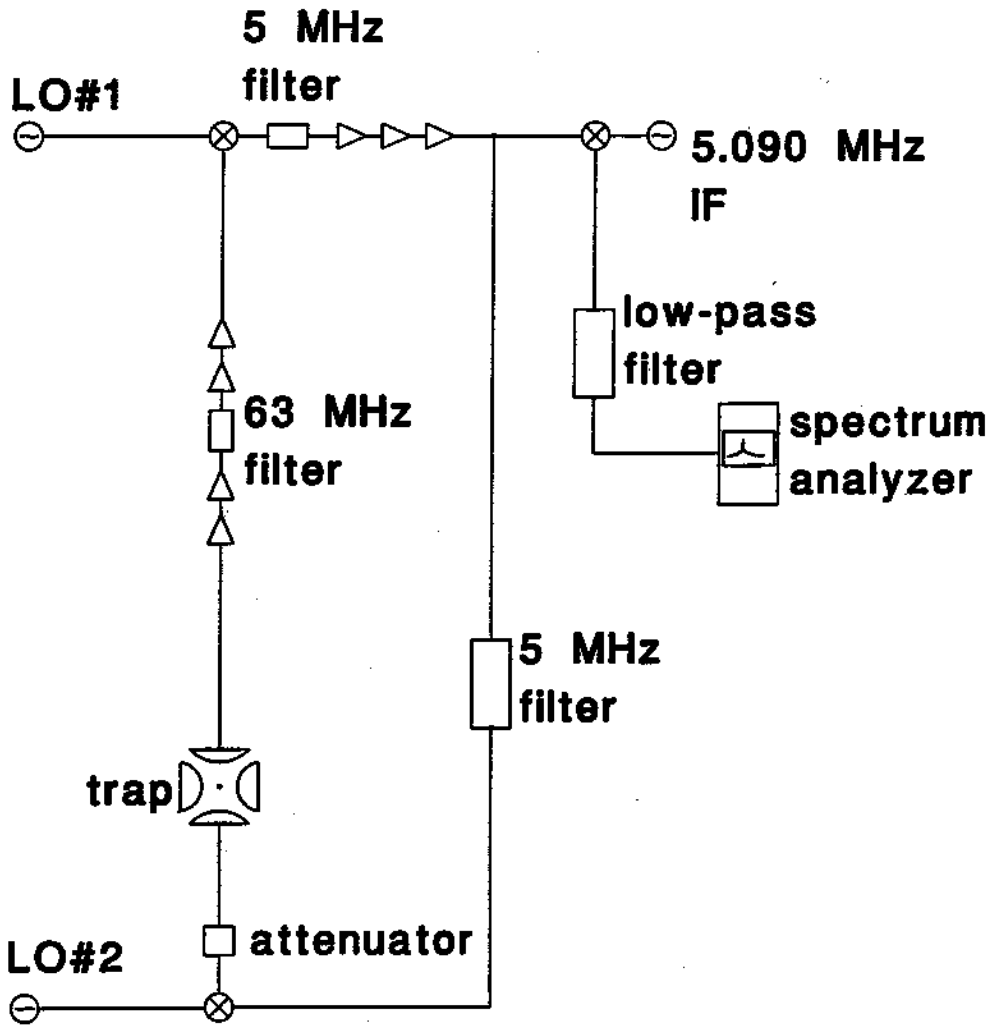

Figure 3.17: Self-excitation schematic. The electron signal is mixed to an appropriate higher frequency and fed back to parametrically drive the electron.

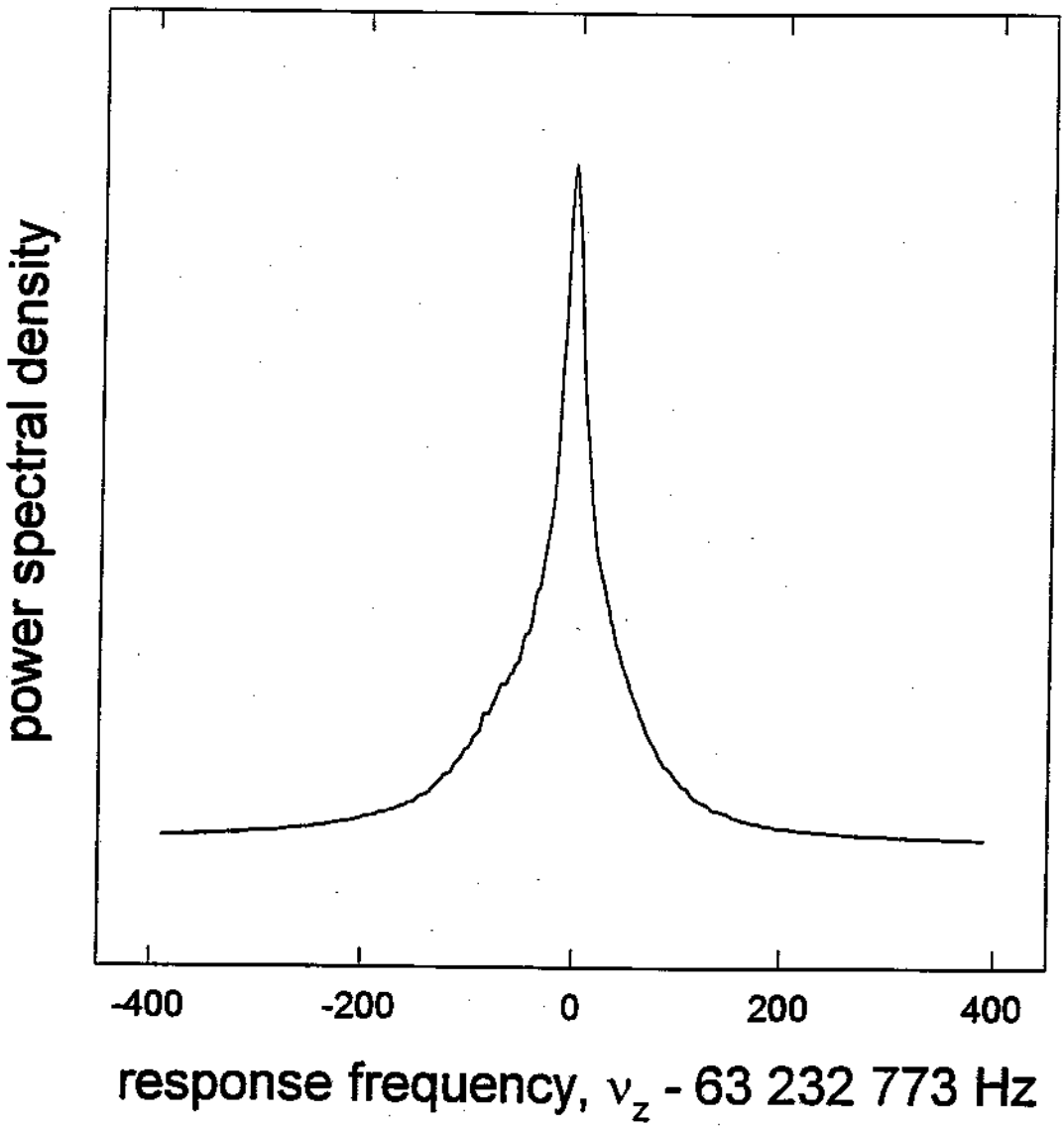

Figure 3.18: Noise excited signal. The particle is excited by noise. The observed full width at half maximum is $\gamma/2\pi = 36$Hz.

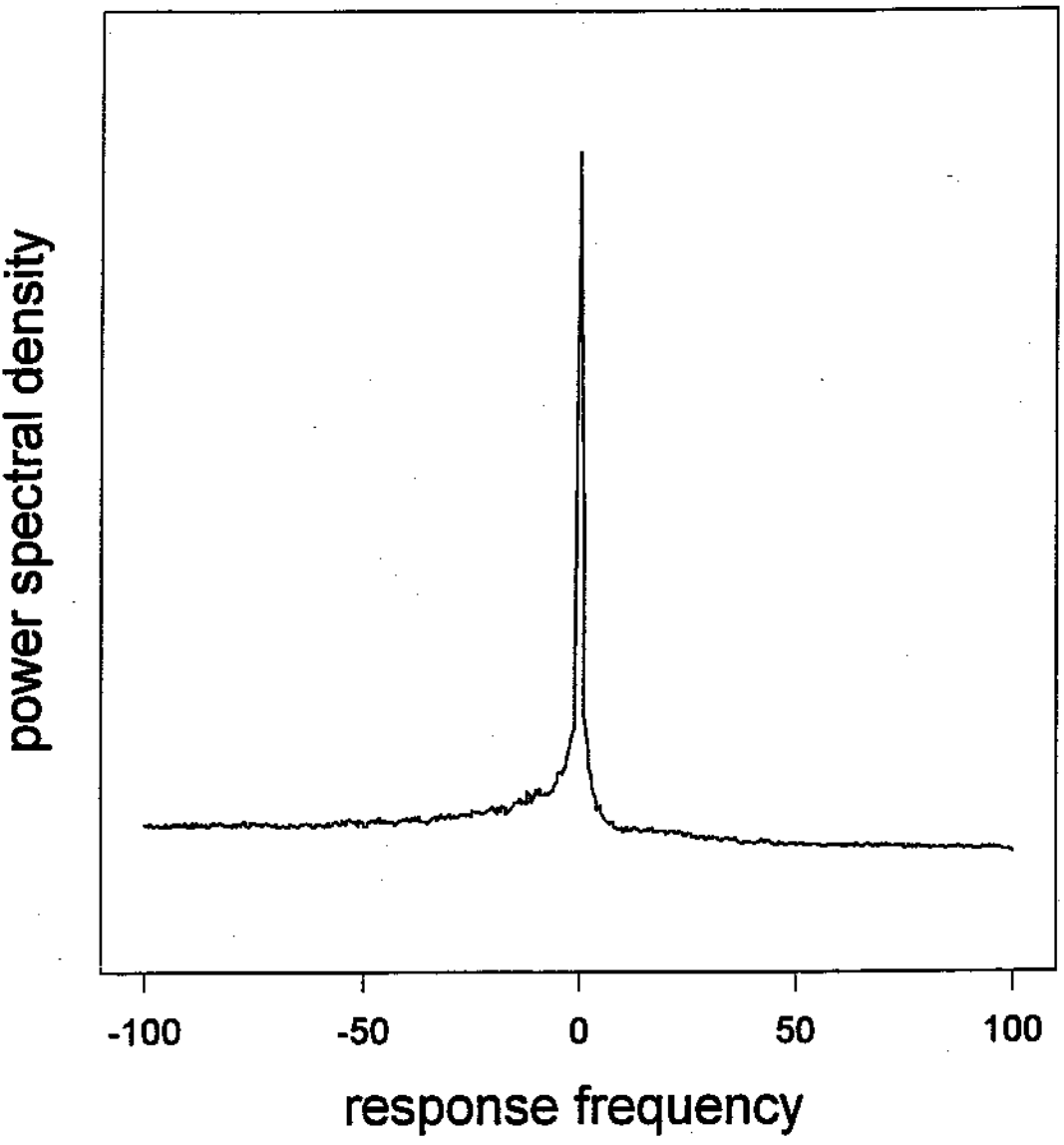

Figure 3.19: Resonant feedback signal. Only one frequency is parametrically resonant after upconversion. This provides a true parametric feedback signal that is filtered. The observed full width at half maximum is $\gamma/2\pi = 1.2$Hz.

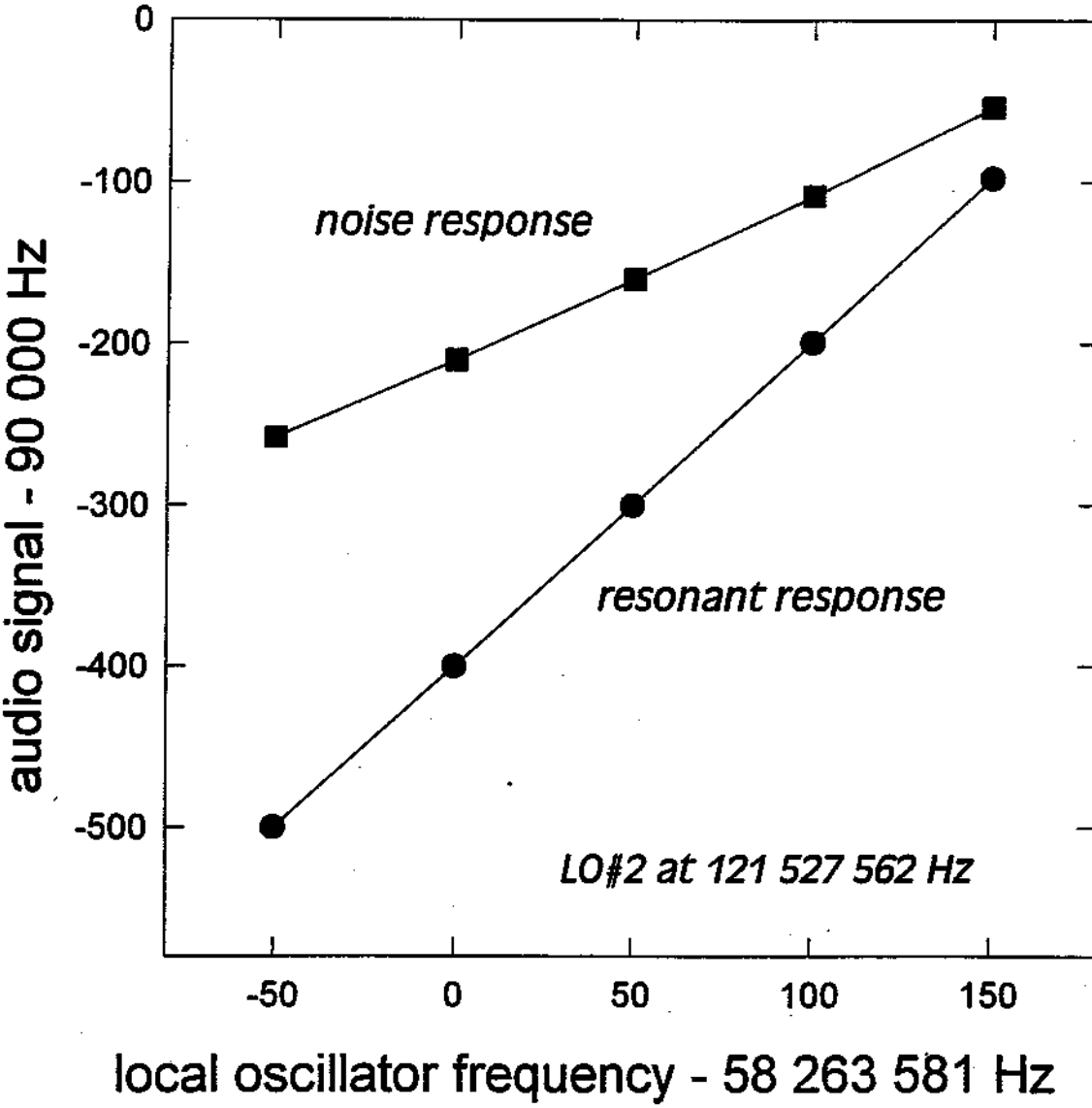

Figure 3.20: Shift in responses as the first local oscillator is varied. The slope of the noise response is 1; while the slope of the resonant response is 2, as expected.

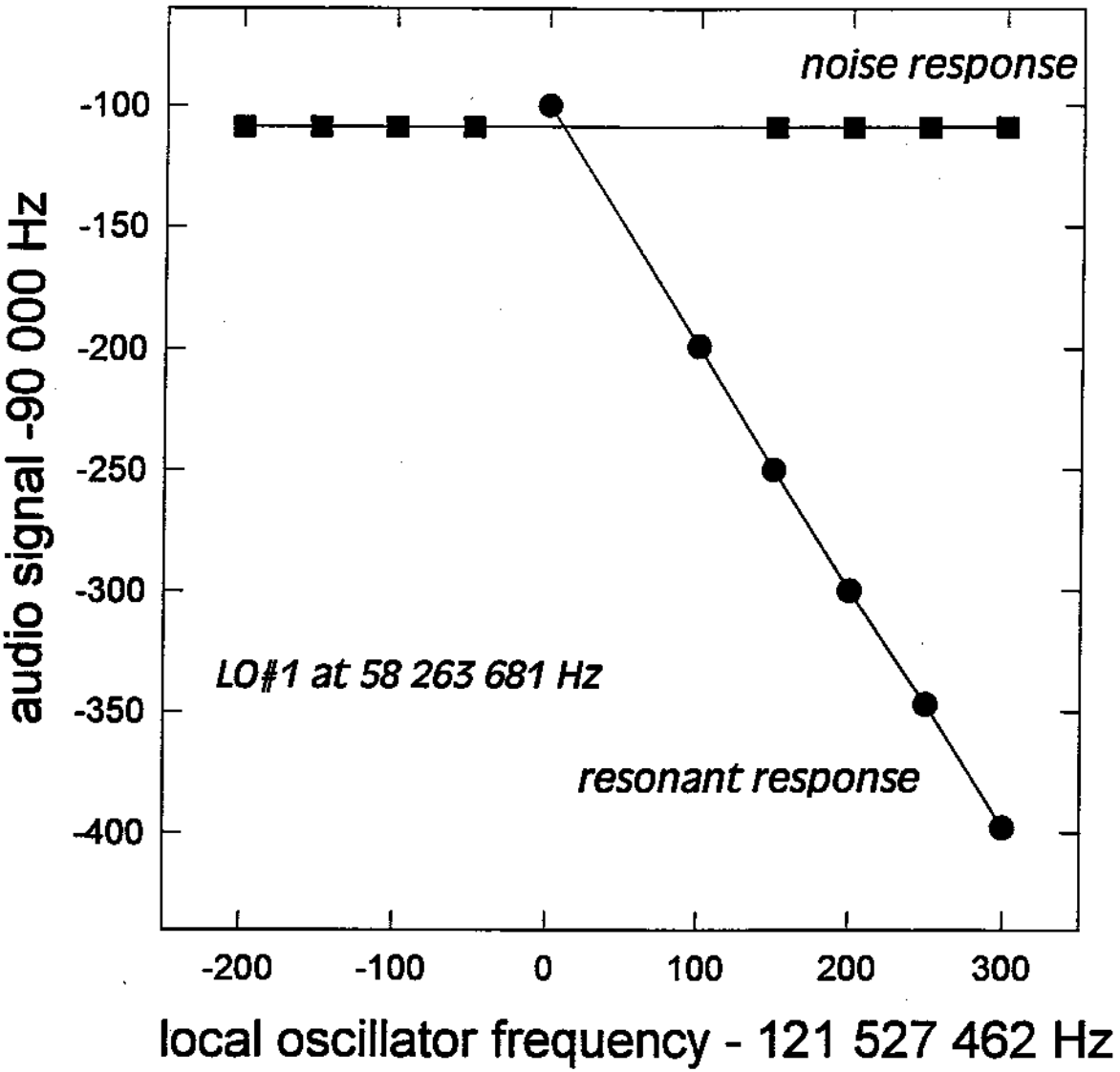

Figure 3.21: Shift in response as the second local oscillator is varied. The noise response shows no dependence; while the resonant response has a slope of -1, as expected.